Cell Reports

Report

Rapid Neuromodulation of Layer 1 Interneurons in Human Neocortex

Graphical Abstract

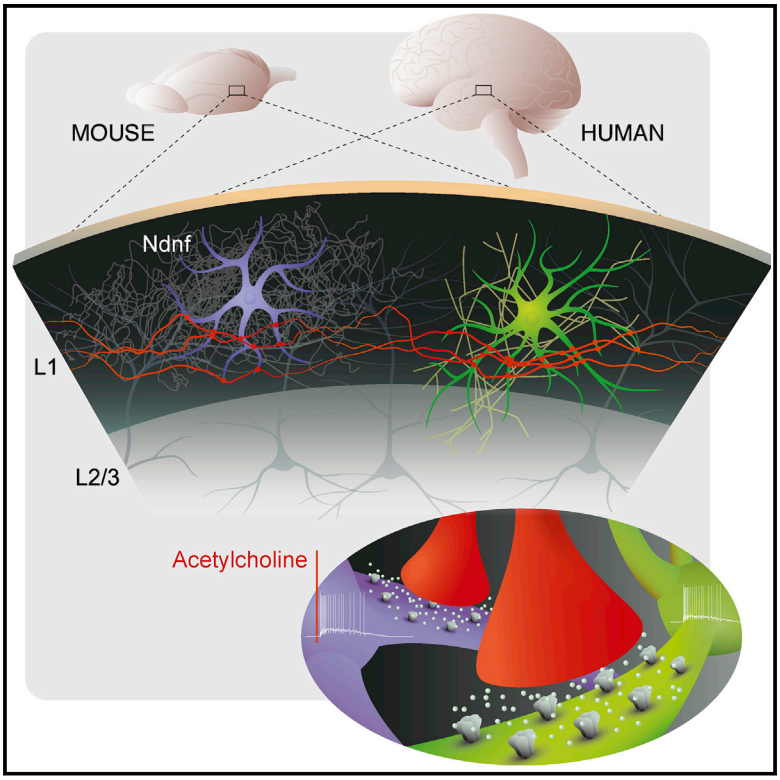

Authors

Rogier B. Poorthuis, Karzan Muhammad, Mantian Wang, ..., Anne Wrana, Huibert D. Mansvelder, Johannes J. Letzkus

Correspondence

johannes.letzkus@brain.mpg.de

In Brief

Inhibitory interneurons govern the function of neural circuits and are in turn controlled by neuromodulation. Here, Poorthuis et al. demonstrate that these mechanisms are conserved in layer 1 of human neocortex, where interneurons express nicotinic acetylcholine receptors that mediate fast responses and thereby enable reconfiguration of circuit function at rapid timescales.

Highlights

- Layer 1 interneurons in human and mouse neocortex respond strongly to acetylcholine
- These rapid responses are mediated by α7 and β2-containing nicotinic receptors
- Human layer 1 comprises neurogliaform cells expressing the conserved marker Ndnf
- Apart from conserved features, human L1 interneurons show a number of specializations

Poorthuis et al., 2018, Cell Reports *23*, 951–958
April 24, 2018
https://doi.org/10.1016/j.celrep.2018.03.111

CellPress

Cell Reports
Report

Rapid Neuromodulation of Layer 1 Interneurons in Human Neocortex

Rogier B. Poorthuis,[1] Karzan Muhammad,[1] Mantian Wang,[1] Matthijs B. Verhoog,[2] Stephan Junek,[1] Anne Wrana,[1] Huibert D. Mansvelder,[2] and Johannes J. Letzkus[1,3,*]
[1]Max Planck Institute for Brain Research, 60438 Frankfurt, Germany
[2]Department of Integrative Neurophysiology, Center for Neurogenomics and Cognitive Research, VU University Amsterdam, De Boelelaan 1085, 1081 HV Amsterdam, the Netherlands
[3]Lead Contact
*Correspondence: johannes.letzkus@brain.mpg.de
https://doi.org/10.1016/j.celrep.2018.03.111

SUMMARY

Inhibitory interneurons govern virtually all computations in neocortical circuits and are in turn controlled by neuromodulation. While a detailed understanding of the distinct marker expression, physiology, and neuromodulator responses of different interneuron types exists for rodents and recent studies have highlighted the role of specific interneurons in converting rapid neuromodulatory signals into altered sensory processing during locomotion, attention, and associative learning, it remains little understood whether similar mechanisms exist in human neocortex. Here, we use whole-cell recordings combined with agonist application, transgenic mouse lines, *in situ* hybridization, and unbiased clustering to directly determine these features in human layer 1 interneurons (L1-INs). Our results indicate pronounced nicotinic recruitment of all L1-INs, whereas only a small subset co-expresses the ionotropic *HTR3* receptor. In addition to human specializations, we observe two comparable physiologically and genetically distinct L1-IN types in both species, together indicating conserved rapid neuromodulation of human neocortical circuits through layer 1.

INTRODUCTION

An ultimate goal of much of modern neuroscience is to understand the function of the human brain, and in particular the human neocortex, which expanded and differentiated substantially during mammalian evolution, mediates many of the capacities that distinguish us from our closest relatives and also plays a central role in psychiatric disorders of human patients (DeFelipe et al., 2002; Marín, 2012; Nelson and Valakh, 2015). Virtually all computations in neocortical circuits are controlled and shaped by the complement of inhibitory interneurons. Different interneuron types show distinct marker expression, physiology, and connectivity with postsynaptic targets and thereby control distinct aspects of circuit function (Kepecs and Fishell, 2014; Wester and McBain, 2014; Poorthuis et al., 2014; Silberberg, 2008). Comparative studies with rodents have revealed that the primate neocortex comprises interneuron types with unique morphologies, along with a greater proportion of interneurons in general and differences in the developmental origin of these cells (DeFelipe et al., 2002; Rakic, 2009). However, despite a few notable exceptions (Jiang et al., 2012; Szegedi et al., 2016; Oláh et al., 2007), we know very little about the physiology and circuit function of distinct human interneuron types.

Here, we take advantage of a well-established source of live slices from human temporal neocortex (Eyal et al., 2016; Verhoog et al., 2013; Testa-Silva et al., 2014) to determine the functional features of human layer 1 interneurons (L1-INs). In rodents, a hallmark of these cells is their strong expression of nicotinic acetylcholine receptors (Christophe et al., 2002; Bennett et al., 2012; Letzkus et al., 2011; Alitto and Dan, 2013; Arroyo et al., 2012), and recent work has shown that these currents are a necessary prerequisite for rapid recruitment of L1-INs, as well as vasoactive intestinal polypeptide (Vip)-expressing cells, by endogenous acetylcholine released during learning, locomotion, and attention (Letzkus et al., 2011; Alitto and Dan, 2013; Pi et al., 2013; Fu et al., 2014; Poorthuis et al., 2014; Letzkus et al., 2015; Kuchibhotla et al., 2017). A second candidate neuromodulator for similar rapid responses is serotonin released from raphe nucleus afferents, which are enriched in layer 1 (Trottier et al., 1996) and thought to predominantly contact interneurons (Chameau and van Hooft, 2006). The HTR3 receptor is the only known fast, ionotropic serotonin receptor, which in rodents is expressed in approximately 10% of L1-INs in frontal cortex (Zhou and Hablitz, 1999), and the majority in somatosensory cortex (Lee et al., 2010). How recruitment by these neuromodulators affects the circuit depends on L1-IN connectivity. Two physiologically and molecularly distinct types of L1-INs have been identified in rodents (Wozny and Williams, 2011; Chu et al., 2003; Tasic et al., 2016; Cruikshank et al., 2012; Zhu and Zhu, 2004), which display differential connectivity in the local circuit (Jiang et al., 2013, 2015) and potentially different functions *in vivo* (Palmer et al., 2012; Letzkus et al., 2015). Here, we determine these attributes in human neocortex and present analogous, age- and area-matched data from wild-type and transgenic mice (see Supplemental Experimental Procedures) to directly link our findings to the large and dynamic rodent literature.

RESULTS

Nicotinic Responses in Human Temporal Neocortex Layer 1 Interneurons

Exploiting the fact that L1-INs can be robustly targeted without genetic markers, we obtained whole-cell recordings in acute slices of healthy human temporal neocortex that needed to be removed to gain access to the underlying pathology and was donated by adult patients (10 male, 3 female, age range 19–52 years, average 36.6 ± 2.9). Layer 1 was identified as the area of low cell density immediately below the pia mater (Figure 1A), and post hoc analyses of neuron density ensured that only neurons located more than 20 μm from the L1/L2 border were included in the dataset.

To address whether human L1-INs express nicotinic receptors, we pressure applied acetylcholine (1 mM) in the presence of the muscarinic antagonist atropine (400 nM). All L1-INs tested in current clamp (n = 12) were depolarized by acetylcholine, with the majority showing suprathreshold responses (8 out of 12 neurons, Figures 1B1 and S1). Voltage-clamp recordings revealed that many L1-INs displayed clearly bi-phasic nicotinic currents (10 out of 21), with a rapid component and a much slower second component (Figure 1B2). The remaining L1-INs had either exclusively slow (n = 8) or fast nicotinic currents (n = 3). Consistent with observations from other areas of rodent cortex (Christophe et al., 2002; Bennett et al., 2012), comparison recordings from temporal neocortex of adult mice produced very similar results (Figures 1 and S1).

To define the nicotinic acetylcholine receptor subtypes mediating these responses, we used pharmacology. In both species, the rapid component of biphasic cholinergic currents was blocked by methyllycaconitine (MLA; 10 nM, Figures 1C, 1D, and S1), identifying α7 receptors as the underlying conductance (Ward et al., 1990). In contrast, the slow component of biphasic currents, and slow monophasic currents were completely abolished by dihydro-beta-erythroidine (DHBE; 1 μM, Figures 1C, 1D, and S1), indicating β2-containing heteromeric receptors (Cordero-Erausquin et al., 2000). The rapid component had a much greater amplitude in general, and in particular in mouse L1-INs (Figure S1), whereas the slow current carried by far most charge in both species (Figures 1C and 1D, cf. Bennett et al., 2012). While the rise time of α7 currents was indistinguishable between human and mouse L1-INs, the slow current displayed both longer rise and decay times in human L1-INs (Figure S1), which may suggest differential modulation or subcellular localization of the receptors or could alternatively be due to morphological differences. Importantly, we could not detect an impact of the patients' smoking history on these currents ($p > 0.05$ for Kruskal-Wallis tests on response amplitude and charge when comparing current or former smokers with non-smokers), in contrast to larger and more prevalent nicotinic currents in layer 6 pyramidal neurons of smokers (Verhoog et al., 2016). Taken together, these results indicate that human L1-INs display strong expression of α7 and β2-containing nicotinic acetylcholine receptors, consistent with similar observations in unidentified human interneurons (Alkondon et al., 2000), and with the high density of nicotine binding sites in human layer 1 (Sihver et al., 1998). Interestingly, fast α7 receptors have been suggested to mediate rapid cholinergic synaptic transmission (Bennett et al., 2012; Smiley et al., 1997), while the slower currents through β2-containing receptors are likely recruited by a form of volume transmission, indicating that a large fraction of L1-INs may thus be recruited by both modes of cholinergic signaling. Together with their pronounced excitability (Figure 3, see below), and the enrichment of cholinergic synapses in human layer 1 (Smiley et al., 1997), our results thus indicate that L1-INs can be rapidly recruited by endogenous acetylcholine release during arousal, attention, and learning in the intact human brain in a fashion similar to that found in behaving mice (Arroyo et al., 2014; Poorthuis et al., 2014; Letzkus et al., 2015).

Conserved Absence of HTR3 Responses in Human Layer 1 Interneurons

A second candidate ionotropic receptor for fast neuromodulation is the serotonin HTR3 receptor, which in rodents is expressed in approximately 10% of L1-INs in frontal cortex (Zhou and Hablitz, 1999), and the majority in somatosensory cortex (Lee et al., 2010). In human L1-INs, pressure application of the selective HTR3 receptor agonist mCPBG (100 μM) yielded no detectable current (Figure 2A, n = 10), and similar results were observed when using serotonin (Figure S2, n = 6). As a control for recording conditions, we verified that acetylcholine elicited robust responses in a subset of these experiments (Figure 2A). Similar to the human data, L1-INs in adult mouse temporal neocortex displayed no response to mCPBG (Figure 2A, n = 10). These data suggest that in both species, the large majority of L1-INs is not under rapid control by serotonin.

However, the number of recordings presented here (n = 26 in total) does not rule out the presence of a small population of responsive L1-INs as reported for rat frontal cortex (Zhou and Hablitz, 1999). Consistent with this, *in situ* hybridization in human and mouse temporal neocortex indicated that, while most *Htr3a* receptor positive neurons are located in layer 2/3, there is also expression in a small set of L1-INs (Figures 2B and S3). We hypothesized that these could be Vip-positive interneurons, which express Htr3a receptors (Férézou et al., 2002; Lee et al., 2010) and represent a small population of L1-INs in mouse neocortex (Prönneke et al., 2015; Xu et al., 2010). Recordings from Vip interneurons in a cross of transgenic mouse lines revealed robust inward currents in response to mCPBG and serotonin both in layer 1 and layer 2/3 (Figures 2C and S2). In contrast, unlabeled, Vip negative L1-INs displayed no response. In line with this result, Vip expression in human and mouse neocortex recapitulates the *Htr3a* profile and is confined to a small population of L1-INs (Figure S3). In conclusion, these data suggest that, while all L1-INs respond to acetylcholine, only the small subset that expresses VIP is under dual control by the serotonergic and cholinergic systems in both species.

Intrinsic Properties of Human Layer 1 Interneurons

The intrinsic physiological properties of human L1-INs determine how neuromodulatory input is converted to circuit modulation by these cells. Our data indicate that human L1-INs (n = 46) display a markedly steeper input-output function compared to the mouse (n = 66), with more than twice the action potential frequency across the whole range of injected current and

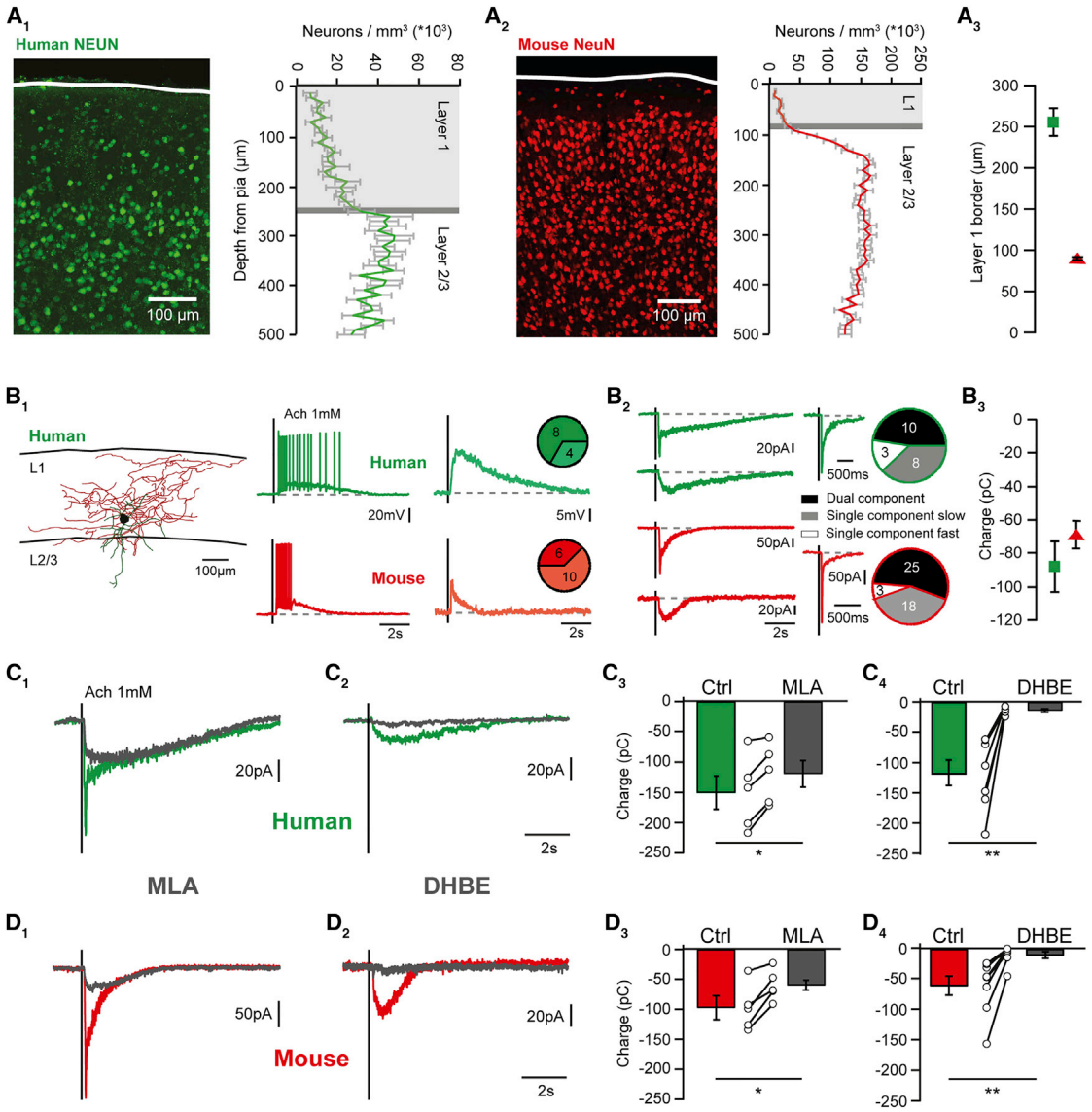

Figure 1. Nicotinic Responses in Human Layer 1 Interneurons

(A) Neuron density relative to the pia was used to define layer 1 in human (green, 7 slices, 3 patients) and mouse neocortex (red, 29 slices, 3 mice) (A_1, A_2). Layer 1 thickness was 254.2 ± 16.3 μm for human and 90.7 ± 2.0 μm for mouse (A_3).

(B) All human and mouse L1-INs showed rapid voltage responses to local pressure application of acetylcholine, and displayed supra- or subthreshold responses in similar proportions (p = 0.25, Fisher's exact test) (B_1). Nicotinic currents showed biphasic time courses in approximately half of the human and mouse cells (top left), with a rapid, large amplitude initial current and a slower second component (B_2). A second major L1-IN fraction displayed exclusively slow currents (bottom left), while the remaining minority showed only the rapid component (center). The proportion of these response types was similar in human and mouse (right, p = 0.58, Fisher exact test). (B_3) The charge of nicotinic responses was similar in the two species (p = 0.39, Kruskal-Wallis test, n = 21 versus n = 46, −88.2 ± 15.5 versus −69.3 ± 8.2 pC).

(C and D) Bath application of the selective α7 receptor antagonist MLA (10 nM) abolished the fast current in human (C_1) and mouse (D_1) L1-INs with biphasic currents. C_3, D_3 MLA reduced the response charge in humans (p < 0.05, n = 5, Wilcoxon signed-rank test, −150.4 ± 27.3 versus −119.2 ± 22.0 pC) and mice (p < 0.05, n = 5, Wilcoxon signed-rank test, −97.6 ± 20.0 versus −60.0 ± 7.9 pC), although its effect on peak amplitude was more pronounced (Figure S1). The β2-containing receptor antagonist DHBE (1 μM) selectively blocked the slow current (C_2, D_2), which carried most of the charge in humans (C_4, p < 0.01, n = 7, Wilcoxon signed-rank test, −118.2 ± 22.7 versus −12.1 ± 2.4 pC, tested on 3 biphasic and 4 monophasic slow currents, see Figure S1) and mice (D_4, p < 0.01, n = 8, Wilcoxon signed-rank test, −66.5 ± 12.0 versus −8.25 ± 4.1 pC, tested on 1 biphasic and 7 monophasic slow currents). Error bars indicate SEM. See also Figure S1.

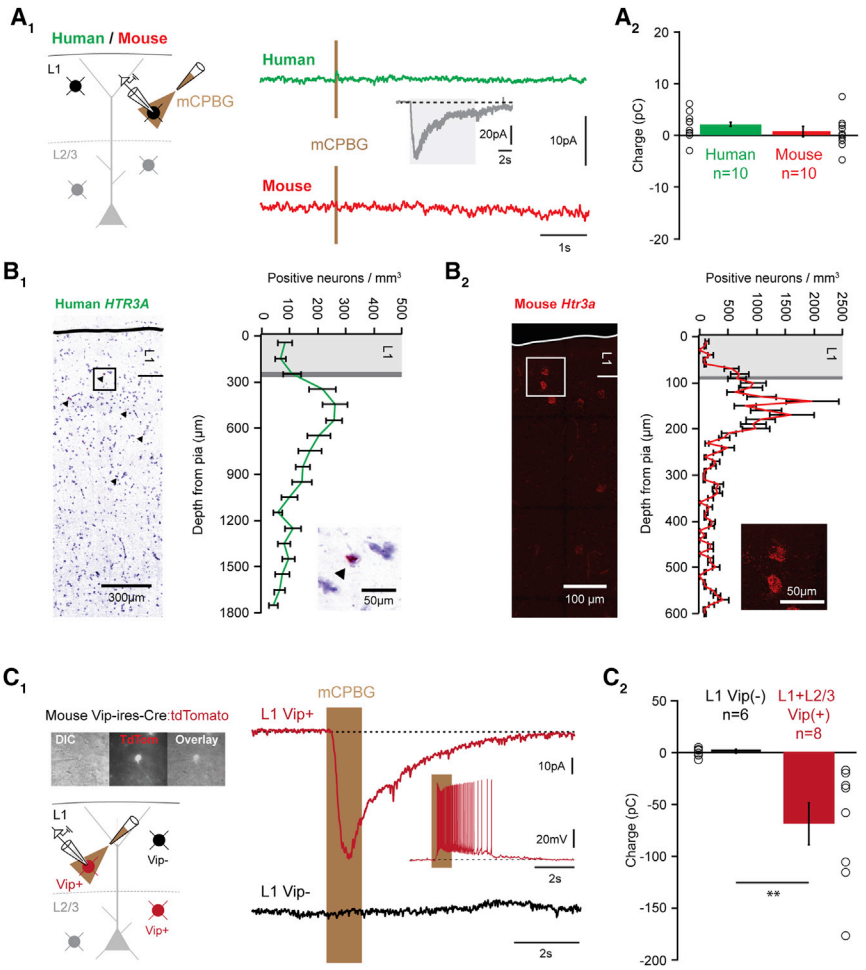

Figure 2. Conserved Absence of HTR3 Responses in Human Layer 1 Interneurons

(A) Pressure application of the selective Htr3 receptor agonist mCPBG (100-ms application displayed, 1 s and 10 s also tested) caused no response in L1-INs of either species, in contrast to robust responses when acetylcholine was applied to the same cells (inset, 10-s application) (A_1). On average, the *Htr3* receptor mediated charge was 1.81 ± 0.82 pC in human (n = 10), and 0.53 ± 1.01 pC in mouse (n = 10), and similar data were obtained with application of serotonin (A_2) (Figure S2).

(B) *In situ* hybridization for *HTR3A* in human (B_1) and mouse neocortex (B_2). Note that while the density peaks in layer 2/3, a small population of positive neurons is also present in layer 1. The image in B_1 is a montage of images assembled using Pannoramic Scan software.

(C) Vip positive interneurons in layer 1 and layer 2/3 were targeted using a cross of transgenic mouse lines. Example responses of a Vip positive and negative L1-IN to mCPBG application. While Vip negative L1-INs showed no response, Vip positive L1-INs and L2-3-INs displayed large inward currents that led to robust firing (inset). Similar data were obtained with application of serotonin (Figure S2) (C_1). The average charge of mCPBG responses in Vip negative L1-INs was 0.13 ± 1.86 pC (n = 6), whereas Vip positive interneurons in layer 1 and layer 2/3 displayed responses of −69.88 ± 0.30 pC (n = 8, $p < 0.01$, Kruskal-Wallis test). Error bars indicate SEM (C_2).

See also Figures S2 and S3.

significantly lower rheobase (Figures 3A–3C and S4). Both higher input resistance and lower action potential threshold of human L1-INs contribute to this effect, while we find no difference in resting membrane potential. In addition, we observe differences in several other intrinsic parameters, including voltage sag and spike frequency accommodation that are of interest for mechanistic models of human neocortex (Figure S4). Importantly, we found no indication that the disease history of human patients had an impact on these results (Figure S4). Consistent with this, greater excitability, lower action potential threshold, and higher input resistance and voltage sag have been reported in a study comparing layer 2/3 neurogliaform cells from healthy macaque and rat (Povysheva et al., 2007). Together, this suggests that these properties represent specializations of certain types of primate interneurons that need to be taken into account when modeling the human neocortex.

Conserved Interneuron Subtypes and Marker Expression in Human Layer 1

Rodent data have shown that L1-INs can be further divided into physiological subtypes (Wozny and Williams, 2011; Chu et al., 2003; Tasic et al., 2016), which display differential connectivity in the local circuit (Jiang et al., 2013, 2015) and potentially different functions *in vivo* (Letzkus et al., 2015). To address whether human L1 comprises similar interneuron subtypes in an unbiased way, we employed unsupervised hierarchical clustering on a comprehensive set of active and passive physiological properties (Figure 3E). For the mouse, this analysis defined two clusters that differ in 7 parameters and correspond to the well-described rodent late-spiking and non-late-spiking L1-INs characterized by differences in latency of the first action potential at rheobase, as well as in spike frequency accommodation, voltage sag, and action potential afterhyperpolarization (Chu et al., 2003; Tasic et al., 2016; Jiang et al., 2013, 2015). The same analysis on human data yielded two clusters that differ in action potential latency, indicating that late-spiking and non-late-spiking interneurons are also present in layer 1 of human neocortex (Figures 3E and 3F). Out of the remaining 9 parameters, 3 showed a corresponding cluster distribution in both species (voltage sag, action potential threshold, membrane time constant), and 2 showed a trend for similarity (input resistance, resting membrane potential), whereas spike frequency accommodation, action potential afterhyperpolarization, and amplitude were clearly distinct between the clusters across species, as well as between human and mouse L1-INs in general (Figure S4). There was no difference in action potential latency between human and mouse late-spiking or non-late-spiking cells ($p > 0.05$, Kruskal-Wallis test). No detectable difference was in addition

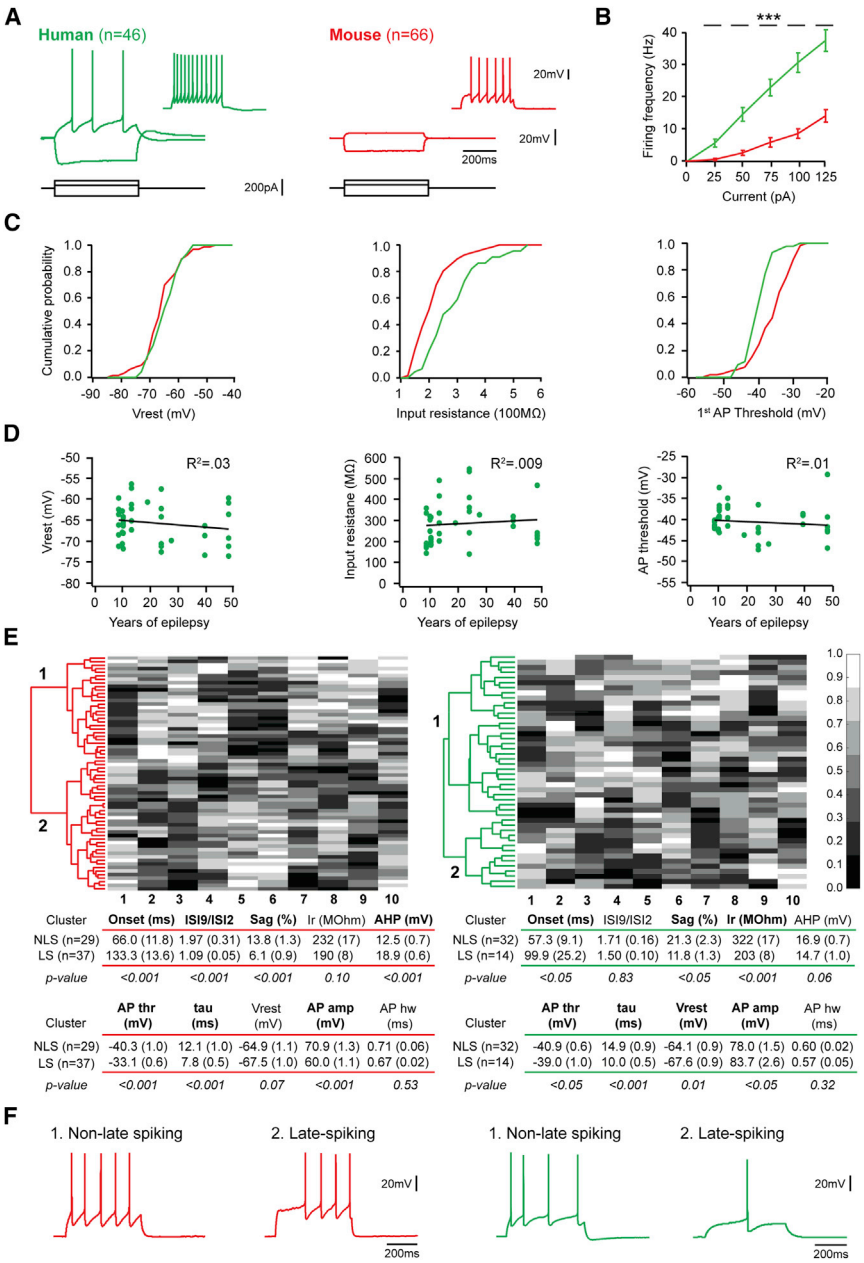

Figure 3. Intrinsic Properties and Subtypes of Human Layer 1 Interneurons

(A) Responses of example human (green) and mouse (red) L1-IN to current injections of −100, +25, and +75 pA (inset).

(B) Human neurons fired at higher frequencies across the entire range of injected currents ($p < 0.001$ for all current amplitudes, Kruskal-Wallis test, n = 46 human neurons and n = 66 mouse neurons).

(C) While the resting membrane potential of human and mouse L1-INs was similar (Vrest, −65.2 ± 0.7 versus −66.4 ± 0.8 mV, Kruskal-Wallis test, $p = 0.28$), human neurons displayed higher input resistance (286.0 ± 14.9 versus 208.4 ± 8.9 MΩ, Kruskal-Wallis test, $p < 0.001$) and lower action potential threshold compared to mice (−40.4 ± 0.5 versus −36.4 ± 0.7 mV, Kruskal-Wallis test, $p < 0.001$), with both factors likely contributing to the greater excitability of human L1-INs.

(D) These parameters showed no correlation with the disease history of the patients ($p > 0.2$, see also Figure S4).

(E) (left) Unsupervised hierarchical clustering on a set of active and passive physiological properties (Ward's method on normalized datasets without prior assumption on cluster number) yielded a non-late-spiking and a late-spiking cluster in the mouse, which also differ in most other parameters (table presents mean, SEM and results of Kruskal-Wallis test). In addition to differences in spiking accommodation, voltage sag, and action potential afterhyperpolarization (Chu et al., 2003; Tasic et al., 2016; Jiang et al., 2013, 2015), the late-spiking L1-INs display more depolarized action potential threshold, faster membrane time constant and lower action potential amplitude. (Right) The same unbiased analysis on human L1-INs yielded similar clusters, with a population of late-spiking cells that display smaller voltage sag, more depolarized action potential threshold, and faster membrane time constant. In addition, input resistance and resting membrane potential displayed similar trends in both species, whereas spiking accommodation, action potential afterhyperpolarization, and amplitude varied in a distinct manner between the two clusters in mouse and human. Calibration bar indicates value rank between 0 and 1.

(F) Example firing patterns. Error bars indicate SEM.

See also Figures S4 and S5.

observed in nicotinic responses between late-spiking and non-late-spiking L1-INs of either species (Figure S5), indicating that both types are under similar cholinergic control. Interestingly, most rodent analyses of late-spiking interneurons have reported little firing accommodation (Chu et al., 2003; Jiang et al., 2013, 2015), potentially suggesting that late-spiking, accommodating L1-INs are a specialization of human neocortex that may be mechanistically related to the larger voltage sag of these cells (Figure S4).

These results indicate that human layer 1 comprises two distinct types of interneurons, which share a range of properties with the respective populations in mice. To address whether this conservation extends to the molecular identity of L1-INs, we utilized neuron-derived neurotrophic factor (Ndnf), a recently described, selective genetic marker for mouse L1 neurogliaform interneurons in visual cortex (Tasic et al., 2016). Intriguingly, *in situ* hybridization revealed that *NDNF*-expressing cells are highly enriched in human layer 1, with a steep drop in density at the border to layer 2 (Figures 4A and S3). Mouse neocortex showed a very similar expression profile (Figures 4A and S3), and we next used a transgenic mouse line expressing eGFP under the Ndnf promoter (Gong et al., 2003) to determine how Ndnf-positive L1-INs relate to the two interneuron subtypes identified in unbiased recordings (Figure 3). Among other properties, Ndnf-positive L1-INs showed long action potential onset latencies, little spiking accommodation, and large action potential afterhyperpolarization (Figures 4B–4D), very similar to the

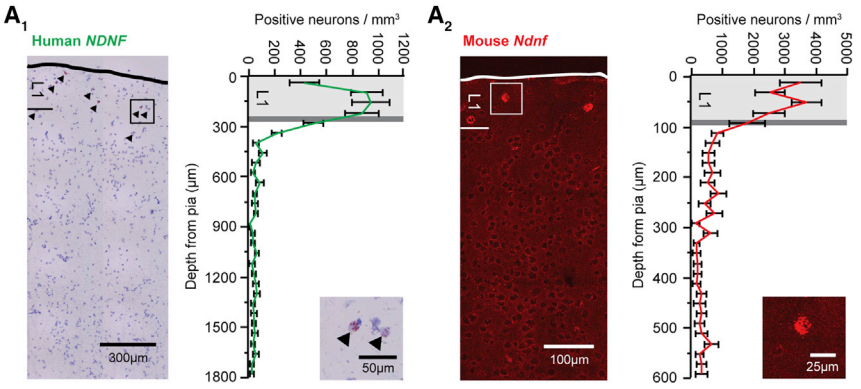

D

Cluster	Onset (ms)	ISI9/ISI2	Sag (%)	Ir (MOhm)	AHP (mV)	AP thr (mV)	tau (ms)	Vrest (mV)	AP amp (mV)	AP hw (ms)
NLS (n=29)	66.0 (11.8)	1.97 (0.31)	13.8 (1.3)	232 (17)	12.5 (0.7)	-40.3 (1.0)	12.1 (1.0)	-64.9 (1.1)	70.9 (1.3)	0.71 (0.06)
LS (n=37)	133.3 (13.6)	1.09 (0.05)	6.1 (0.9)	190 (8)	18.9 (0.6)	-33.1 (0.6)	7.8 (0.5)	-67.5 (1.0)	60.0 (1.1)	0.67 (0.02)
NDNF (n=15)	154.0 (37.3)	1.11 (0.09)	8.1 (1.9)	169 (11)	18.2 (1.1)	-35.1 (1.1)	8.6 (0.7)	-67.7 (1.4)	62.4 (1.9)	0.66 (0.02)
NLS vs LS	*<0.001*	*<0.001*	*<0.001*	*0.10*	*<0.001*	*<0.001*	*<0.001*	*0.07*	*<0.001*	*0.53*
Ndnf vs NLS	*0.01*	*<0.001*	*0.02*	*0.02*	*<0.001*	*<0.01*	*<0.01*	*0.08*	*<0.01*	*0.57*
Ndnf vs LS	*0.69*	*0.99*	*0.54*	*0.26*	*0.75*	*0.12*	*0.2*	*0.75*	*0.38*	*0.9*

Figure 4. Neuron-Derived Neurotrophic Factor Is a Conserved Marker for Human Layer 1 Neurogliaform Cells

(A) *In situ* hybridization for *NDNF* in human neocortex (left) and quantification of the distribution of positive neurons along cortical depth (12 slices from 2 patients). The density of *NDNF*-positive neurons is high in layer 1 (light gray) and drops off steeply at the border to layer 2 (dark gray) (A_1). *In situ* hybridization for *Ndnf* in mouse temporal neocortex (16 slices from 3 animals) shows a similar expression profile, indicating that *Ndnf* is a conserved marker for layer 1 interneurons (A_2). The image in A_1 is a montage of images assembled using Pannoramic Scan software.

(B) Whole-cell current-clamp slice recording using an Ndnf-eGFP mouse line.

(C) To determine whether Ndnf positive layer 1 interneurons correspond to one of the populations identified by unbiased clustering of the entire layer 1 interneuron population (Figure 3), we compared the distribution of action potential onset (C_1), spiking accommodation (C_2), and action potential afterhyperpolarization (C_3) in the three populations. Ndnf interneurons display robust similarity with the late-spiking cluster in all three parameters.

(D) Statistical comparison of the 10 attributes used for clustering between the three populations indicates that Ndnf interneurons and cells in the late-spiking cluster differ from the non-late-spiking cluster in the same properties, whereas no difference could be detected between the late-spiking and Ndnf populations. Error bars indicate SEM.

late-spiking cluster. Moreover, a quantitative comparison revealed that Ndnf-positive L1-INs differ from the non-late-spiking cluster in the same properties as the late-spiking cluster, whereas no differences between Ndnf-positive L1-INs and the late-spiking cluster were found (Figures 4B–4D). The observed convergence between marker expression and clustering as two independent approaches provides strong evidence that late-spiking L1-INs are Ndnf-positive neurogliaform cells and highlights the power and sensitivity of a clustering approach based on a comprehensive set of properties. Taken together, these data indicate that human neocortex expresses a conserved marker for L1 neurogliaform cells and comprises a population of late-spiking interneurons, suggesting that human layer 1 contains a set of neurogliaform cells or a physiologically and genetically related interneuron type. In turn, identification of NDNF will facilitate future research on these interneurons, for instance, by enabling postmortem analyses in different brain disorders and more precise translation of mouse data to the human brain.

DISCUSSION

Layer 1 is the unique site in neocortex where a variety of long-range projections from cortical, higher-order thalamic and neuromodulatory sources impinges onto the apical dendrites of local pyramidal neurons and the sparse set of L1-INs (Cauller, 1995; Douglas and Martin, 2004). In line with this organization, recent data from rodents indicate that L1-INs in sensory cortex are specialized for encoding contextual information such as primary reinforcers (Letzkus et al., 2011), interhemispheric interactions (Palmer et al., 2012), and multimodal processing (Ibrahim et al., 2016). While a mechanistic understanding of such processes in the human brain is still elusive, our aim here was first to determine the functional properties of human L1-INs and second to test to what extent data from the mouse—where further rapid progress is expected due to a range of high-resolution *in vivo* approaches—is relevant to the function of human neocortex. In contrast to recent studies reporting differences between human and rodent pyramidal neurons in terms of membrane properties (Eyal et al., 2016), synaptic plasticity (Verhoog et al., 2013), and communication (Testa-Silva et al., 2014), our results indicate that key properties of L1-INs at the level of physiology, marker expression, and neuromodulation are conserved in human neocortex. This suggests that, despite the striking evolution of neocortical structure, and particularly of the inhibitory system (DeFelipe et al., 2002), L1-INs carry out comparable functions in the two species. However, future work is required to elucidate whether human non-late-spiking L1-INs show similarities to the single-bouquet cells found in the rodent (Jiang et al., 2013, 2015). In addition, it will be important to determine whether the two human L1-IN types can be further subdivided based on additional markers, morphological properties, and connectivity (Tasic et al., 2016; Jiang et al., 2015). Moreover, our data also reveal differences between human and mouse L1-INs, which together with a previous study comparing layer 2/3

neurogliaform interneurons between macaque and rat (Povysheva et al., 2007) identify specializations of these interneuron types in the primate brain such as the greater voltage sag that can profoundly affect their physiological properties.

In addition to the evolutionary relevance, a more precise understanding of the physiology of different identified human interneurons types is also a key prerequisite for biomedical research. Maladaptive changes in both inhibitory interneurons (Marín, 2012; Nelson and Valakh, 2015) and cholinergic neuromodulation (Levin, 2013) are thought to be core features of a range of human brain disorders and the present results together with the available data on human fast-spiking interneurons and neurogliaform cells in deeper layers (Jiang et al., 2012; Szegedi et al., 2016; Oláh et al., 2007) also provide a first framework for a cell-type-specific, mechanistic understanding of the underlying pathophysiology that can be used to build quantitative disease models and to evaluate the relevance of data obtained in other model systems such as tissue derived from induced pluripotent stem cells.

EXPERIMENTAL PROCEDURES

Further details and an outline of resources used in this work can be found in Supplemental Experimental Procedures. All procedures on mice were performed in accordance with institutional guidelines and were approved by the Regierungspräsidium Darmstadt. All procedures on human tissue were performed with the approval of the Medical Ethical Committee of the VU University Medical Centre, and in accordance with Dutch license procedures and the declaration of Helsinki.

Brain Slice Preparation and Patch-Clamp Recordings

Healthy human brain tissue was obtained from anterior medial temporal cortex with written informed consent of patients undergoing surgical treatment (10 male, 3 female, age range 19–52 years, age 36.6 ± 2.9 years). Experimental mice (85 ± 5 days, age range 40–162 days) of both sexes were sacrificed by decapitation under anesthesia. Brain slices were prepared using standard procedures. Whole-cell recordings were performed at 31°C–34°C, and agonists were pressure-applied to the soma of the recorded neuron.

Analysis of Intrinsic Properties and Interneuron Subtypes

Neurons were subjected to current steps (500 ms, −100 to 250 pA), and passive and active properties were determined from the resulting voltage traces. Unsupervised clustering was performed on ranked data using Ward's method.

In Situ Hybridization and Immunohistochemistry

In situ hybridization and immunohistochemistry was performed using fluorescent labeling in mouse tissue and chromogenic staining in human cortex according to standard procedures. Cells were detected and their location relative to the pia mater was determined.

Statistics

Datasets were tested for normality (Kolmogorov-Smirnov test) and subjected to the tests indicated in the text. A result was considered significant when the p value was lower than 0.05. Since effect size was unknown, sample size could not be pre-specified. No randomization procedure or blinding of experimenter was used in the experimental design.

SUPPLEMENTAL INFORMATION

Supplemental Information includes Supplemental Experimental Procedures and five figures and can be found with this article online at https://doi.org/10.1016/j.celrep.2018.03.111.

ACKNOWLEDGMENTS

We thank all members of the Letzkus lab, Erin Schuman, Maria Sol Fustinana Gueler, Julijana Gjorgjieva, and members of the FENS Kavli Network of Excellence for comments and discussions, Or Shahar for help with *in situ* hybridization, Ioannis Kramvis for help with human slicing, Brigitte Sinke and Hans Lodder for outstanding technical assistance, Florian Vollrath for expert help with image processing, Friedrich Kretschmer and Georgi Tushev for assistance with programming and data analysis, and Julia Kuhl for artwork. This work was supported by the Max Planck Society, the European Research Council (StG 335587 to J.J.L.), the German Research Foundation (CRC 1193 – B02 to J.J.L.), the Minna James Heineman Foundation (to J.J.L.), and the Netherlands Organization for Scientific Research (NWO Rubicon, 825.13.015 to R.B.P.).

AUTHOR CONTRIBUTIONS

R.B.P. and J.J.L. initiated the project, R.B.P. performed most experiments, K.M., M.W., A.W., and M.B.V. performed experiments, R.B.P., S.J., and J.J.L. performed data analyses. R.B.P. and J.J.L. conceived the project and wrote the manuscript with input from H.D.M. All authors contributed to the experimental design and interpretation and commented on the manuscript.

DECLARATION OF INTERESTS

The authors declare no competing interests.

Received: November 9, 2017
Revised: February 8, 2018
Accepted: March 25, 2018
Published: April 24, 2018

REFERENCES

Alitto, H.J., and Dan, Y. (2013). Cell-type-specific modulation of neocortical activity by basal forebrain input. Front. Syst. Neurosci. *6*, 79.

Alkondon, M., Pereira, E.F., Eisenberg, H.M., and Albuquerque, E.X. (2000). Nicotinic receptor activation in human cerebral cortical interneurons: A mechanism for inhibition and disinhibition of neuronal networks. J. Neurosci. *20*, 66–75.

Arroyo, S., Bennett, C., Aziz, D., Brown, S.P., and Hestrin, S. (2012). Prolonged disynaptic inhibition in the cortex mediated by slow, non-α7 nicotinic excitation of a specific subset of cortical interneurons. J. Neurosci. *32*, 3859–3864.

Arroyo, S., Bennett, C., and Hestrin, S. (2014). Nicotinic modulation of cortical circuits. Front. Neural Circuits *8*, 30.

Bennett, C., Arroyo, S., Berns, D., and Hestrin, S. (2012). Mechanisms generating dual-component nicotinic EPSCs in cortical interneurons. J. Neurosci. *32*, 17287–17296.

Cauller, L. (1995). Layer I of primary sensory neocortex: Where top-down converges upon bottom-up. Behav. Brain Res. *71*, 163–170.

Chameau, P., and van Hooft, J.A. (2006). Serotonin 5-HT(3) receptors in the central nervous system. Cell Tissue Res. *326*, 573–581.

Christophe, E., Roebuck, A., Staiger, J.F., Lavery, D.J., Charpak, S., and Audinat, E. (2002). Two types of nicotinic receptors mediate an excitation of neocortical layer I interneurons. J. Neurophysiol. *88*, 1318–1327.

Chu, Z., Galarreta, M., and Hestrin, S. (2003). Synaptic interactions of late-spiking neocortical neurons in layer 1. J. Neurosci. *23*, 96–102.

Cordero-Erausquin, M., Marubio, L.M., Klink, R., and Changeux, J.P. (2000). Nicotinic receptor function: New perspectives from knockout mice. Trends Pharmacol. Sci. *21*, 211–217.

Cruikshank, S.J., Ahmed, O.J., Stevens, T.R., Patrick, S.L., Gonzalez, A.N., Elmaleh, M., and Connors, B.W. (2012). Thalamic control of layer 1 circuits in prefrontal cortex. J. Neurosci. *32*, 17813–17823.

DeFelipe, J., Alonso-Nanclares, L., and Arellano, J.I. (2002). Microstructure of the neocortex: Comparative aspects. J. Neurocytol. *31*, 299–316.

Douglas, R.J., and Martin, K.A. (2004). Neuronal circuits of the neocortex. Annu. Rev. Neurosci. *27*, 419–451.

Eyal, G., Verhoog, M.B., Testa-Silva, G., Deitcher, Y., Lodder, J.C., Benavides-Piccione, R., Morales, J., DeFelipe, J., de Kock, C.P., Mansvelder, H.D., and Segev, I. (2016). Unique membrane properties and enhanced signal processing in human neocortical neurons. eLife *5*, 1–18.

Férézou, I., Cauli, B., Hill, E.L., Rossier, J., Hamel, E., and Lambolez, B. (2002). 5-HT3 receptors mediate serotonergic fast synaptic excitation of neocortical vasoactive intestinal peptide/cholecystokinin interneurons. J. Neurosci. *22*, 7389–7397.

Fu, Y., Tucciarone, J.M., Espinosa, J.S., Sheng, N., Darcy, D.P., Nicoll, R.A., Huang, Z.J., and Stryker, M.P. (2014). A cortical circuit for gain control by behavioral state. Cell *156*, 1139–1152.

Gong, S., Zheng, C., Doughty, M.L., Losos, K., Didkovsky, N., Schambra, U.B., Nowak, N.J., Joyner, A., Leblanc, G., Hatten, M.E., and Heintz, N. (2003). A gene expression atlas of the central nervous system based on bacterial artificial chromosomes. Nature *425*, 917–925.

Ibrahim, L.A., Mesik, L., Ji, X.Y., Fang, Q., Li, H.F., Li, Y.T., Zingg, B., Zhang, L.I., and Tao, H.W. (2016). Cross-Modality Sharpening of Visual Cortical Processing through Layer-1-Mediated Inhibition and Disinhibition. Neuron *89*, 1031–1045.

Jiang, M., Zhu, J., Liu, Y., Yang, M., Tian, C., Jiang, S., Wang, Y., Guo, H., Wang, K., and Shu, Y. (2012). Enhancement of asynchronous release from fast-spiking interneuron in human and rat epileptic neocortex. PLoS Biol. *10*, e1001324.

Jiang, X., Wang, G., Lee, A.J., Stornetta, R.L., and Zhu, J.J. (2013). The organization of two new cortical interneuronal circuits. Nat. Neurosci. *16*, 210–218.

Jiang, X., Shen, S., Cadwell, C.R., Berens, P., Sinz, F., Ecker, A.S., Patel, S., and Tolias, A.S. (2015). Principles of connectivity among morphologically defined cell types in adult neocortex. Science *350*, aac9462.

Kepecs, A., and Fishell, G. (2014). Interneuron cell types are fit to function. Nature *505*, 318–326.

Kuchibhotla, K.V., Gill, J.V., Lindsay, G.W., Papadoyannis, E.S., Field, R.E., Sten, T.A., Miller, K.D., and Froemke, R.C. (2017). Parallel processing by cortical inhibition enables context-dependent behavior. Nat. Neurosci. *20*, 62–71.

Lee, S., Hjerling-Leffler, J., Zagha, E., Fishell, G., and Rudy, B. (2010). The largest group of superficial neocortical GABAergic interneurons expresses ionotropic serotonin receptors. J. Neurosci. *30*, 16796–16808.

Letzkus, J.J., Wolff, S.B., Meyer, E.M., Tovote, P., Courtin, J., Herry, C., and Lüthi, A. (2011). A disinhibitory microcircuit for associative fear learning in the auditory cortex. Nature *480*, 331–335.

Letzkus, J.J., Wolff, S.B., and Lüthi, A. (2015). Disinhibition, a circuit mechanism for associative learning and memory. Neuron *88*, 264–276.

Levin, E.D. (2013). Complex relationships of nicotinic receptor actions and cognitive functions. Biochem. Pharmacol. *86*, 1145–1152.

Marín, O. (2012). Interneuron dysfunction in psychiatric disorders. Nat. Rev. Neurosci. *13*, 107–120.

Nelson, S.B., and Valakh, V. (2015). Excitatory/inhibitory balance and circuit homeostasis in autism spectrum disorders. Neuron *87*, 684–698.

Oláh, S., Komlósi, G., Szabadics, J., Varga, C., Tóth, E., Barzó, P., and Tamás, G. (2007). Output of neurogliaform cells to various neuron types in the human and rat cerebral cortex. Front. Neural Circuits *1*, 4.

Palmer, L.M., Schulz, J.M., Murphy, S.C., Ledergerber, D., Murayama, M., and Larkum, M.E. (2012). The cellular basis of GABA(B)-mediated interhemispheric inhibition. Science *335*, 989–993.

Pi, H.J., Hangya, B., Kvitsiani, D., Sanders, J.I., Huang, Z.J., and Kepecs, A. (2013). Cortical interneurons that specialize in disinhibitory control. Nature *503*, 521–524.

Poorthuis, R.B., Enke, L., and Letzkus, J.J. (2014). Cholinergic circuit modulation through differential recruitment of neocortical interneuron types during behaviour. J. Physiol. *592*, 4155–4164.

Povysheva, N.V., Zaitsev, A.V., Kröner, S., Krimer, O.A., Rotaru, D.C., Gonzalez-Burgos, G., Lewis, D.A., and Krimer, L.S. (2007). Electrophysiological differences between neurogliaform cells from monkey and rat prefrontal cortex. J. Neurophysiol. *97*, 1030–1039.

Prönneke, A., Scheuer, B., Wagener, R.J., Möck, M., Witte, M., and Staiger, J.F. (2015). Characterizing VIP neurons in the barrel cortex of VIPcre/tdTomato mice reveals layer-specific differences. Cereb. Cortex *25*, 4854–4868.

Rakic, P. (2009). Evolution of the neocortex: A perspective from developmental biology. Nat. Rev. Neurosci. *10*, 724–735.

Sihver, W., Gillberg, P.G., and Nordberg, A. (1998). Laminar distribution of nicotinic receptor subtypes in human cerebral cortex as determined by [3H](-)nicotine, [3H]cytisine and [3H]epibatidine in vitro autoradiography. Neuroscience *85*, 1121–1133.

Silberberg, G. (2008). Polysynaptic subcircuits in the neocortex: Spatial and temporal diversity. Curr. Opin. Neurobiol. *18*, 332–337.

Smiley, J.F., Morrell, F., and Mesulam, M.M. (1997). Cholinergic synapses in human cerebral cortex: An ultrastructural study in serial sections. Exp. Neurol. *144*, 361–368.

Szegedi, V., Paizs, M., Csakvari, E., Molnar, G., Barzo, P., Tamas, G., and Lamsa, K. (2016). Plasticity in single axon glutamatergic connection to GABAergic interneurons regulates complex events in the human neocortex. PLoS Biol. Published online November 9, 2016. https://doi.org/10.1371/journal.pbio.2000237.

Tasic, B., Menon, V., Nguyen, T.N., Kim, T.K., Jarsky, T., Yao, Z., Levi, B., Gray, L.T., Sorensen, S.A., Dolbeare, T., et al. (2016). Adult mouse cortical cell taxonomy revealed by single cell transcriptomics. Nat. Neurosci. *19*, 335–346.

Testa-Silva, G., Verhoog, M.B., Linaro, D., de Kock, C.P., Baayen, J.C., Meredith, R.M., De Zeeuw, C.I., Giugliano, M., and Mansvelder, H.D. (2014). High bandwidth synaptic communication and frequency tracking in human neocortex. PLoS Biol. Published online November 25, 2014. https://doi.org/10.1371/journal.pbio.1002007.

Trottier, S., Evrard, B., Vignal, J.P., Scarabin, J.M., and Chauvel, P. (1996). The serotonergic innervation of the cerebral cortex in man and its changes in focal cortical dysplasia. Epilepsy Res. *25*, 79–106.

Verhoog, M.B., Goriounova, N.A., Obermayer, J., Stroeder, J., Hjorth, J.J., Testa-Silva, G., Baayen, J.C., de Kock, C.P., Meredith, R.M., and Mansvelder, H.D. (2013). Mechanisms underlying the rules for associative plasticity at adult human neocortical synapses. J. Neurosci. *33*, 17197–17208.

Verhoog, M.B., Obermayer, J., Kortleven, C.A., Wilbers, R., Wester, J., Baayen, J.C., De Kock, C.P., Meredith, R.M., and Mansvelder, H.D. (2016). Layer-specific cholinergic control of human and mouse cortical synaptic plasticity. Nat. Commun. *7*, 12826.

Ward, J.M., Cockcroft, V.B., Lunt, G.G., Smillie, F.S., and Wonnacott, S. (1990). Methyllycaconitine: A selective probe for neuronal alpha-bungarotoxin binding sites. FEBS Lett. *270*, 45–48.

Wester, J.C., and McBain, C.J. (2014). Behavioral state-dependent modulation of distinct interneuron subtypes and consequences for circuit function. Curr. Opin. Neurobiol. *29*, 118–125.

Wozny, C., and Williams, S.R. (2011). Specificity of synaptic connectivity between layer 1 inhibitory interneurons and layer 2/3 pyramidal neurons in the rat neocortex. Cereb. Cortex *21*, 1818–1826.

Xu, X., Roby, K.D., and Callaway, E.M. (2010). Immunochemical characterization of inhibitory mouse cortical neurons: Three chemically distinct classes of inhibitory cells. J. Comp. Neurol. *518*, 389–404.

Zhou, F.M., and Hablitz, J.J. (1999). Activation of serotonin receptors modulates synaptic transmission in rat cerebral cortex. J. Neurophysiol. *82*, 2989–2999.

Zhu, Y., and Zhu, J.J. (2004). Rapid arrival and integration of ascending sensory information in layer 1 nonpyramidal neurons and tuft dendrites of layer 5 pyramidal neurons of the neocortex. J. Neurosci. *24*, 1272–1279.

Cell Reports, Volume *23*

Supplemental Information

Rapid Neuromodulation of Layer 1 Interneurons in Human Neocortex

Rogier B. Poorthuis, Karzan Muhammad, Mantian Wang, Matthijs B. Verhoog, Stephan Junek, Anne Wrana, Huibert D. Mansvelder, and Johannes J. Letzkus

Supplemental Information

Supplemental Figures

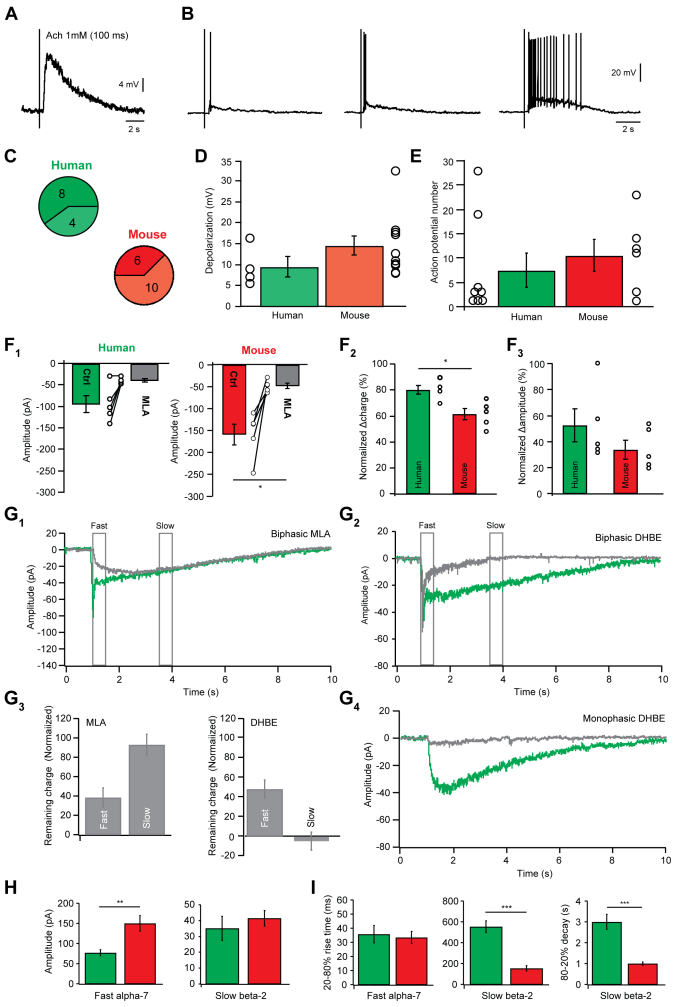

Figure S1: Nicotinic voltage responses and pharmacology of human and mouse layer 1 interneurons. Related to Figure 1.

Example subthreshold (**A**) and suprathreshold voltage responses in human L1-INs (**B**). **C** Proportion of subthreshold (light color) and suprathreshold (dark color) responses in human (green) and mouse L1-INs (red). **D** Average amplitude of subthreshold responses in human (n=4, 9.56±2.4 mV) and mouse L1-INs (n=10, 14.6±2.2 mV, p=0.09, Kruskal-Wallis test). **E** Number of action potentials elicited in human (n=8, 7.5±3.6 APs) and mouse L1-INs (n=6, 10.7±3.3 APs). These data indicate similar recruitment of L1-INs in the two species by acetylcholine. **F_1** The selective α7 receptor antagonist MLA (10 nM) strongly reduced the peak amplitude of biphasic nicotinic currents in human (n=5, p=0.06, Wilcoxon signed rank test, 94.1±8.8 versus 40.0±3.2 pA) and mouse L1-INs (n=5, p=0.01, Wilcoxon signed rank test, 159.1±24.1 versus 48.0±6.2 pA). **F_2** The MLA-sensitive α7 receptor response contributed relatively less charge to biphasic currents in human compared to mouse (p=0.01, Kruskal-Wallis test, n=5 each, 79.9±3.2 versus 61.8±4.5%). **F_3** In contrast, the relative amplitude was affected similarly in the two species (p=0.17, Kruskal-Wallis test, n=5 each, 52.6±12.9 versus 33.2±7.0%). **G_1** Average trace (n=5 neurons) displaying the effect of MLA on biphasic

currents in human cells. MLA strongly reduces the charge in the early phase of the nicotinic current but not in the late phase, consistent with the kinetics of α7 nicotinic receptors that are characterized by a fast activation onset and rapid desensitization. **G_2** Average trace (n=3) displaying the effect of DHBE on biphasic currents. DHBE strongly reduces the late component of human nicotinic currents while leaving the rapid component intact, indicating that the late component is mediated by β2-containing nicotinic receptors that are characterized by slow kinetics. **G_3** Quantification of the effect of MLA and DHBE on the early and late component of nicotinic currents indicated in **G_1** and **G_2**. MLA greatly reduced the charge in the early phase (38.4±9.9 % remaining charge) but did not affect the late phase of the current (93.5±10.6 % remaining charge). DHBE also effected the early phase of the nicotinic current (47.7±9.6% remaining charge), indicating that consistent with the trace in **G_1**, at this time point the response is mediated by both receptor types. In contrast to MLA, however, DHBE completely abolished the late component (-5.41±9.1% remaining charge). These data indicate that a subset of human layer 1 neurons expresses two different types of nicotinic receptors. **G_4** Complete block of slow monophasic responses in human cells (n=4) by DHBE. **H** The amplitude of α7 currents was larger in mouse compared to human L1-INs (left, p<0.01, Kruskal-Wallis test, human n=13, mouse n=28, 77.0±7.2 versus 150.5±19.5 pA). In contrast, β2-containing receptor currents displayed similar amplitudes in both species (right, p=0.70, Kruskal-Wallis test, human n=8, mouse n=18, 35.2±7.4 versus 41.4±4.9 pA). **I** The rise time of α7 currents did not differ between human and mouse L1-INs (left, p=0.99, Kruskal-Wallis test, human n=13, mouse n=28, 35.8±6.3 versus 33.6±4.3 ms). In contrast, β2-containing receptor currents displayed both slower rise (center, p<0.001, Kruskal-Wallis test, human n=8, mouse n=18, 554.5±75.4 versus 165.3±25.4 ms) and decay times in human recordings (right, p<0.001, Kruskal-Wallis test, human n=18, mouse n=43, 2.88±0.33 versus 1.01±0.08 s). This difference may be due to differential modulation of receptor kinetics, differential sub-cellular localization of the receptors or differences in L1-IN morphologies between the species. Error bars indicate s.e.m.

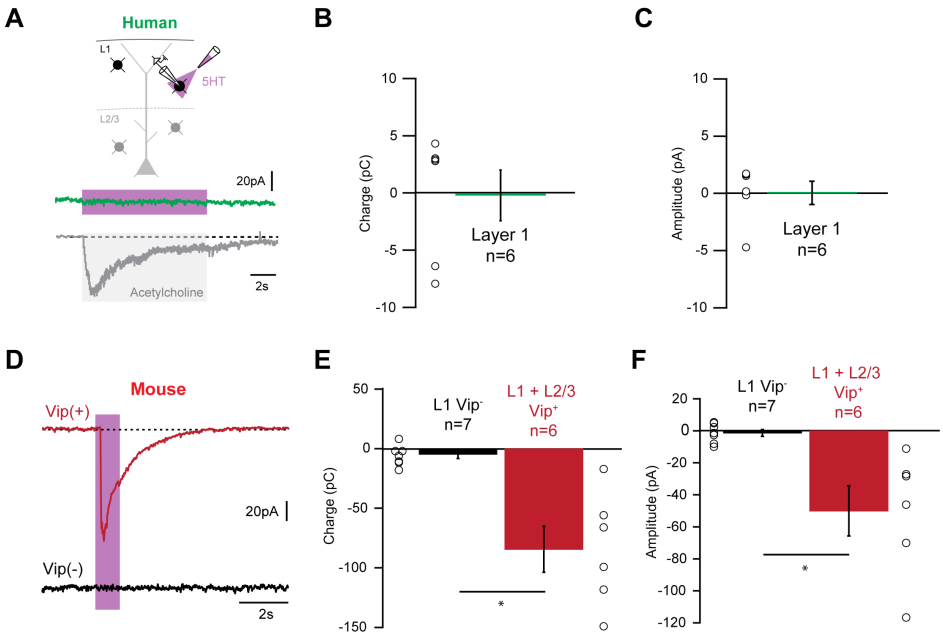

Figure S2: Serotonin responses in human and mouse layer 1 interneurons. Related to Figure 2.

A Experimental setup for pressure application of 5-HT (100 µM) for 10s. 5-HT elicited no detectable response in human L1-INs (**B**, **C**, n=6), in contrast to robust responses when acetylcholine was applied to the same cells (inset in **A**, 10s application). **D** Example responses of a Vip positive and a Vip negative L1-IN to 5-HT (1s, 100 µM). While Vip negative L1-INs showed no response, Vip positive interneurons in layer 1 and layer 2/3 displayed large inward currents. **E** The average charge of 5-HT responses in Vip negative L1-INs was -4.69±3.63 pC (n=7), whereas Vip positive interneurons in layer 1 and layer 2/3 displayed responses of -84.35±19.43 pC (n=6, $p<0.01$, Kruskal-Wallis test). **F** The average amplitude of 5-HT responses in Vip negative L1-INs was -1.32±2.14 pA (n=7), whereas Vip positive interneurons in layer 1 and layer 2/3 displayed responses of -50.08±15.68 pA (n=6, $p<0.01$, Kruskal-Wallis test). Together with data in **Figure 2**, this indicates that within layer 1, 5-HT controls exclusively the small population of interneurons that expresses Vip. Error bars indicate s.e.m.

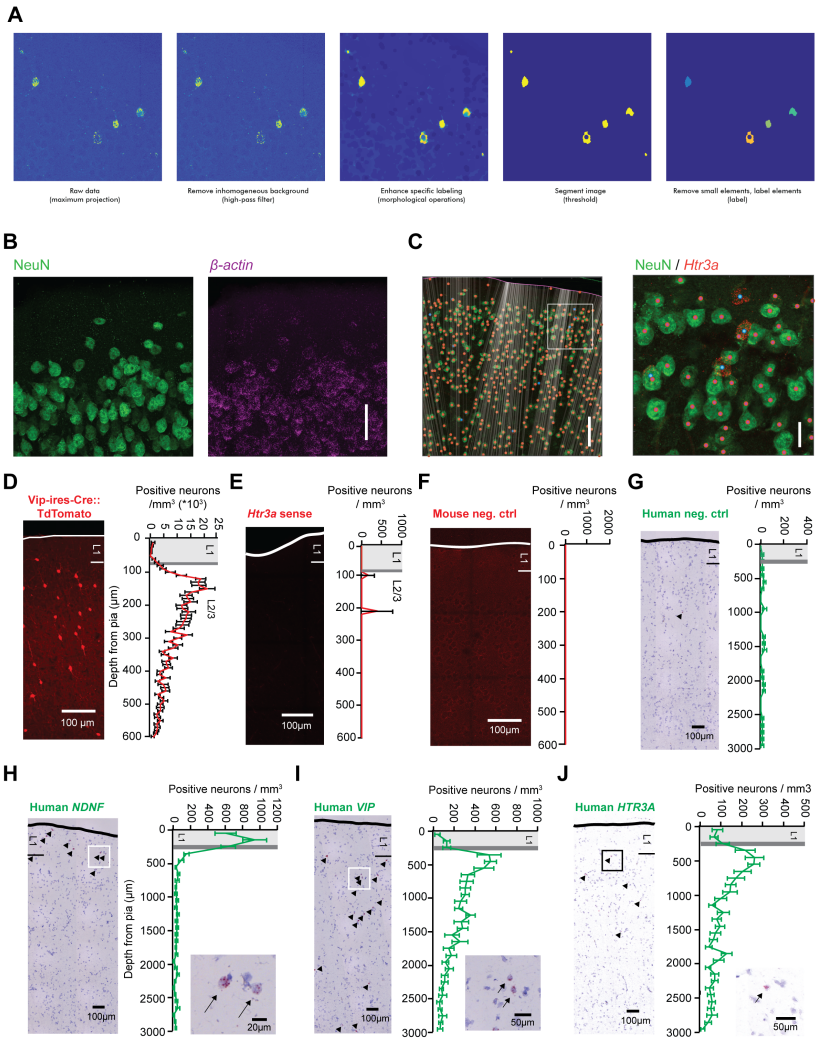

Figure S3: In situ hybridization for HTR3A receptors, VIP and NDNF in human and mouse temporal cortex. Related to Figure 2 and 4.

A Operations performed on fluorescent *in situ* images to convert the punctate staining to identification of positive neurons (see Methods for details). **B** Slice of mouse temporal cortex showing layer 1 and layer 2/3 neurons stained for the neuronal marker NeuN (**left**) and β-actin mRNA (**right**). Note detection of mRNA in layer 1 neurons (scale bar 50 µm). **C left** Neurons were automatically detected in the NeuN channel, and their distance to the pia was determined by drawing a line to the closet point on the pia (scale bar 100 µm). **C right** Automatically detected neurons in the NeuN channel are depicted as red dots. *Htr3a* mRNA positive cells detected by the analysis algorithm are labeled with a blue dot. The punctate mRNA staining was fused by the operation shown in **A** to identify positive neurons in an unbiased fashion (scale bar 20 µm). **D right** Vip interneurons were visualized using Vip-ires-cre mice (Taniguchi et al., 2011) crossed with a tdTomato reporter line (Ai9, Madisen et al., 2010). **Left** Density of Vip interneurons as a function of distance from the pia (n=3 mice, 29 slices). **E** Control experiment with a sense probe for *Htr3a* receptor mRNA showed virtually no false positive cells (n=3 mice, 7 slices). **F** Control experiment for mouse *Ndnf in situ* with a negative probe (6 slices from 3 mice). **G to J** Due to the strong autofluorescence of human tissue, we performed chromogenic rather than fluorescent *in situ* hybridization. **G** Control experiment for human *in situ* shows little unspecific labeling (5 slices from 2 patients). **H** Slice of human temporal cortex showing chromogenic *in situ* hybridization for *NDNF*, and quantification of expression profile along the depth in cortex (same as **Figure 4**, displayed

here for comparison, 12 slices from 2 patients). **I** Expression of *VIP* is low in layer 1, and shows a peak in upper layer 2 (10 slices from 2 patients), similar to the expression profile in mouse neocortex (**Figure 2**). **J** Expression of *HTR3A* receptors resembles that of *VIP*, consistent with co-localization of these markers (same as **Figure 2**, displayed here for comparison 9 slices from 2 patients). Together, these data indicate that in both species *NDNF* is a selective marker for layer 1 interneurons, that *VIP* and *HTR3A* receptors are restricted to a small subset of L1-INs, and that they potentially co-localize as our recordings in the mouse suggest (**Figure 2**). Error bars indicate s.e.m. The images in panels **G** to **J** are a montage of images stitched using Pannoramic Scan software.

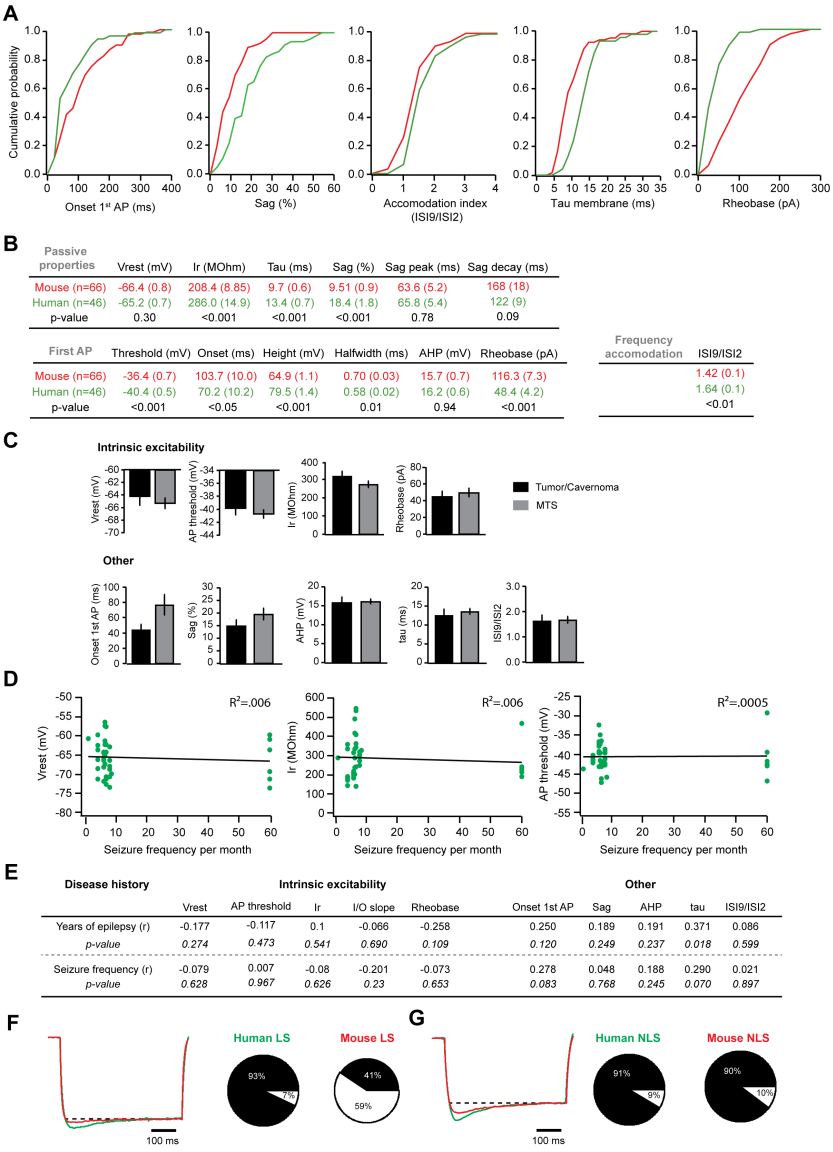

Figure S4: Cellular properties of human and mouse layer 1 interneurons, and further analyses of the impact of* disease type or disease history of the human patients. *Related to Figure 3.

Cumulative distributions (**A**) and table (**B**) summarizing the electrophysiological properties of human (n=46) and mouse (n=66) layer 1 interneurons (**B:** all values are presented as mean and s.e.m., p-values are the result of Kruskal-Wallis tests). We observed differences between human and mouse L1-INs in a number of parameters: Human L1-INs displayed higher input resistance, slower membrane time constant, larger voltage sag as determined by the percentage difference between the steady-state and peak voltage during a hyperpolarizing current step, more hyperpolarized action potential threshold, shorter onset of firing the first action potential at rheobase, greater action potential amplitude, faster action potential kinetics, lower rheobase and a higher level of accommodation during trains of action potentials (>20 Hz) as determined by dividing the 9th inter-spike interval by the second. **C** Data from patients with mesial temporal sclerosis (light grey, 36 neurons from 8 patients) and from patients which had epilepsy as a result of tissue malformation (tumor or cavernoma, dark grey, 10 neurons from 3 patients) were compared. No significant differences were found for the different parameters investigated between these groups (Vrest: -65.4±0.8 vs -64.1±1.6

mV, p=0.44; AP threshold: -40.6±0.6 vs -39.7±1.1 mV, p=0.39; input resistance: 277.2±16.7 vs 317.5±27.1 MΩ, p=0.14; rheobase: 49.3±5.1 vs 45±6.2 pA, p=0.99; onset latency 1st AP: 77.4±12.7 vs 44.5±6.8 ms, p=0.39; sag: 19.3±2.2 vs 15.0±2.4 %, p=0.5; AHP: 14.3±1.5 vs 15.8±1.5 mV, p=0.61; membrane time constant: 13.7±0.8 vs 12.5±1.6 ms; ISI9/ISI2: 1.64±0.13 vs 1.64±0.23, p=0.99). **D** We addressed the potential influence of disease severity on intrinsic excitability of layer 1 neurons. Correlations between seizure frequency per month and intrinsic excitability showed only very weak, non-significant correlations (resting membrane potential: R^2 =0.006, p=0.63, input resistance: R^2 =0.006, p=0.63, AP threshold: R^2 =0.0005, p=0.97). **E** Table summarizing correlations between neuronal parameters and disease state. With the exception of membrane time constant, we observe no correlation between disease history and intrinsic properties. This suggests that disease history is unlikely to have a major impact on the results. **F** A notable difference between human and mouse late-spiking cells is the larger voltage sag (p<0.001, Kruskal-Wallis test, human n=14, mouse n=37, 11.8±1.3 versus 6.1±0.9 %). Traces on the left are normalized to steady-state voltage to illustrate this. In addition, the proportion of late-spiking cells with a voltage sag >5% was also significantly greater in human L1-INs (black, p<0.01, Fisher's exact test). **G** While human non-late-spiking cells also showed larger voltage sag (left, p<0.01, Kruskal-Wallis test, human n=32, mouse n=29, 21.3±2.3 versus 13.8±1.3 %), the proportion of cells with a voltage sag >5% was similar for both species (black, p=0.99, Fisher's exact test). Error bars indicate s.e.m.

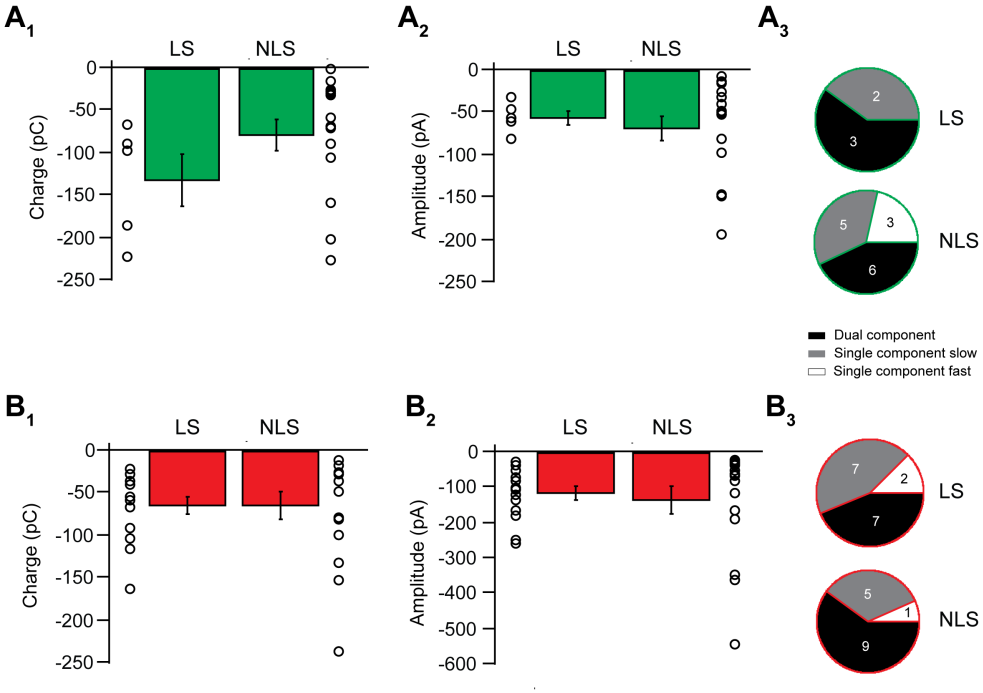

Figure S5: Nicotinic responses in non-late-spiking and late-spiking layer 1 interneurons. Related to Figure 3.

Nicotinic receptor responses were grouped for non-late-spiking (NLS) and late-spiking (LS) L1-INs (hierarchical clustering using Ward's method, **Figure 3**), and analyzed for charge, amplitude and receptor composition. **A_1, A_2** In the human, LS and NLS neurons showed similar response charge and amplitude (p=0.21, Kruskal-Wallis test, n=5 versus n=14, -133.0±29.9 pC versus -80.4±18.8 pC, and p=0.78, Kruskal-Wallis test, -56.4±8.2 versus -68.9±15.6 pA). **B_1, B_2** Similar analysis for mouse L1-INs. Comparable to the human, there was no detectable difference between LS and NLS cells (p=0.38, Kruskal-Wallis test, n=15 versus n=16, -65.0±10.9 versus -66.4±15.8 pC, and p=0.45, Kruskal-Wallis test, -117.6±18.0 versus -137.5±38.7 pA). **A_3, B_3:** Nicotinic response types found on late-spiking and non-late-spiking L1-INs. There was no detectable difference in the relative proportions of dual, single fast and single slow component responses in either species (human: p=0.58, mouse: p=0.72, Fisher exact test). Error bars indicate s.e.m.

Supplemental Experimental Procedures

Contact for reagent and resource sharing

Further information and requests for resources and reagents should be directed to and will be fulfilled by the lead contact, Johannes Letzkus (johannes.letzkus@brain.mpg.de).

Experimental model and subject details

Human brain tissue

Human brain tissue was obtained from 13 patients (10 male, 3 female, age range 19-52 years, age 36.6±2.9 years). Patients were either diagnosed with, and treated for, mesial temporal sclerosis (n=10), a brain tumor (n=2) or cavernoma (n=1). Healthy human brain tissue was obtained from anterior medial temporal cortex that had to be removed for surgical access to deeper brain structures (see below), with written informed consent of the patients before surgery.

Mouse brain tissue

Experimental mice (85±5 days, age range 40 to 162 days) of both sexes were either wildtype C57Bl6/J transgenes obtained from a cross of Vip-ires-cre (Taniguchi et al., 2011) with conditional tdTomato reporter animals (Ai9, Madisen et al., 2010) in C57Bl6/J background or NDNF-eGFP mice (Gong et al., 2003) in C57Bl6/J background. Mice were maintained in a 12 hour light/dark cycle, with access to food and water *ad libitum*.

Human slice preparation

All procedures on human tissue were performed with the approval of the Medical

Ethical Committee of the VU University Medical Centre, and in accordance with Dutch license procedures and the declaration of Helsinki. Human brain slices were cut from anterior medial temporal cortex tissue that had to be removed to provide surgical access to deeper brain structures, with written informed consent of the patients before surgery, as described previously (Testa-Silva et al., 2014). While precise information on the localization of the excised tissue was not available, the human anterior medial temporal cortex as a whole is an associative, multimodal area involved in associative learning. On this basis, as well as on the basis of homologous localization in as far as that is possible despite the expansion of temporal association areas during evolution (Squire et al., 2004), we performed comparison recordings from mouse temporal association cortex (TeA) and neighboring secondary auditory cortex (AuV, according to Paxinos and Franklin, 2008) as in previous work (Verhoog et al., 2013). We obtained tissue from 13 patients (10 male, 3 female, age 36.6±2.9 years). Patients were either diagnosed with, and treated for, mesial temporal sclerosis (n=10), a brain tumor (n=2) or cavernoma (n=1). In all patients, the resected neocortical tissue was located well outside the epileptic focus or tumor, and displayed no structural abnormalities in preoperative MRI investigations. Anesthesia was induced with fentanyl (1–3 µg/kg, i.v.) and a bolus dose of propofol (2–10 mg/kg), and was maintained with remyfentanyl (250 µg/kg/min) and propofol (4–12 mg/kg). After resection, the cortical tissue was placed within 30 s in ice-cold artificial CSF (aCSF) slicing solution, which contained the following (in mM): 110 choline chloride, 26 NaHCO3, 10 D-glucose, 11.6 sodium ascorbate, 7 MgCl2, 3.1 sodium pyruvate, 2.5 KCl, 1.25 NaH2PO4, and 0.5 CaCl2. The tissue was then transported to the neurophysiology laboratory, which is located within 200 m of the operating room. Transition time between resection of tissue and slice preparation was <10 min. Cortical slices (350 µm thick) were prepared in ice-cold slicing solution, and transferred to holding chambers in which they were stored for 30 min at 34°C and subsequently for at least 1 h at room temperature All aCSF solutions were

continuously bubbled with carbogen gas (95% O2, 5%CO2), and had an osmolality of 300 mOsm.

Mouse slice preparation

Experimental mice were either wildtype C57Bl6/J, or transgenes obtained from a cross of Vip-ires-cre (Taniguchi et al., 2011) and conditional tdTomato reporter animals (Ai9, Madisen et al., 2010) in C57Bl6/J background. Mice were maintained in a 12 hour light/dark cycle, with access to food and water *ad libitum*. All animal procedures were performed in accordance with institutional guidelines and were approved by the Regierungspräsidium Darmstadt. To ensure comparability to the human data, slices were obtained from temporal association cortex (TeA) and secondary auditory cortex (AuV, coordinates from bregma according to Paxinos and Franklin (2008): 2 to 3.2mm posterior, 4 to 4.5mm lateral, 2.5 to 3.6mm ventral) of adult male and female mice (85±5 days, age range 40 to 162 days). All recordings made to study nicotinic receptor currents used slicing solutions as reported above for human slice preparation. Slices in which serotonergic currents were studied were made using standard aCSF solution containing (in mM) 125 NaCl, 26 NaHCO3, 10 D-glucose, 7 MgCl2, 3 KCl, 1.25 NaH2PO4, and 0.5 CaCl2.

Patch-clamp recordings in human and mouse slices

Slices were transferred to the recording chamber and perfused with aCSF (2-3 mL/min). All experiments were performed at 31-34°C. Cells were visualized using differential interference contrast microscopy. Whole-cell voltage-clamp and current-clamp recordings were made using Multiclamp 700B amplifiers (Axon Instruments, CA), low-pass filtered at 5 to 20 kHz and digitized at 10 to 50 kHz (Digidata 1550, Molecular Devices) using pClamp software (Molecular Devices). Recordings were

rejected or terminated when the access resistance exceeded 20 MΩ. Patch pipettes (3-6 MΩ) were pulled from standard-wall borosilicate capillaries and were filled with intracellular solution (in mM): 140 K-gluconate, 1 KCl, 10 4-(2-hydroxyethyl)-1-piperazineethanesulfonic acid, 4 Na-phosphocreatine, 4 ATP-Mg, 0.4 GTP and biocytin (4 mg/mL). pH was adjusted to 7.3 with KOH, and osmolality was 290-300 mOsm. Layer 1 was identified by the lower cell density compared to layer 2/3. The L1/L2 border was defined by binning neuron density (bin size 10 µm), and identifying the last bin before the neuronal density exceeded 1 standard deviation above the average of the first 250 µm for 3 consecutive bins in human slices, and above the average of the first 80 µm for 2 consecutive bins for mouse tissue. To avoid recording neurons from a mixed L1-L2 population, cells were only recorded if they were located >20 µm from the L2 border, which was verified in a subset of the experiments by post hoc staining for NeuN and biocytin. TdTomato labeled Vip neurons were visualized under epifluorescence using an LED (565 nm, Cool LED) and a CCD camera (Infinity3, Lumenera). When the whole-cell configuration was established, hyperpolarizing and depolarizing current steps of 500 ms duration were injected, starting at -100 pA with a step increment of 25 pA. From this data passive and active properties of the neuron were determined offline. Series resistance was left uncompensated, and values were not corrected for the liquid junction potentials. Fast ionotropic receptor currents on interneurons were tested in voltage clamp mode (-70 mV holding potential) by local pressure ejection of agonists from a glass pipette with a tip diameter of approximately 1 µm using either a Picospritzer III (General valve corporation, Fairfield, NJ) or a PDES-02DE-LA-2 pressure ejection system (NPI, Germany). Nicotinic currents were evoked by a 100 ms puff of acetylcholine chloride (Ach, 1 mM) with a pressure of 10psi. Despite the fact that rodent L1-INs display gap junction coupling (Chu et al., 2003, Tasic et al., 2016), previous research indicates that electrical synapses contribute little to nicotinic currents in L1-INs (Bennett et al., 2012, Chu et al., 2003), suggesting that the observed responses are

mediated by nicotinic receptors in the recorded neuron. Htr3 currents were tested using mChlorophenylbiguanide hydrochloride (mCPBG, 100μM, in a subset of mouse experiments depicted in **Figure 2** the concentration of mCPBG was changed to 1μM (n=2) or 10μM (n=2)), and application lasted 100 ms in mouse and human experiments. In a subset of human recordings in **Figure 2**, mCPBG was applied for either 1 or 10 seconds. In the experiment where L1 Vip negative and Vip positive cells are compared for modulation by Htr3 receptors, mCPBG and serotonin hydrochloride (5HT) were applied for 1 second. 5HT (100μM) was applied to human cells for a duration of 10 s. In a subset of human cells that did not show a depolarizing current to mCPBG or 5HT, nicotinic responses were tested and found in all cases. For 100 ms application the puffer pipette was located approximately 20 μm from the soma, while for longer application times the distance was increased to approximately 30-50 μm. All experiments were performed in the presence of DNQX (10 μM) and bicuculline freebase (1 μM) to block glutamatergic and GABAergic synaptic transmission. We note that while bicuculline freebase at very high concentrations has been reported to block small-conductance calcium-activated potassium channels in addition to ionotropic GABA receptors (IC_{50} > 46μM) (Khawaled et al., 1999), our main aim here was a species comparison and given that bicuculline was present in all mouse and human recordings this does not have a major impact on the comparability of these data-sets. The presence of atropine (400 nM) prevented stimulation of muscarinic receptors during acetylcholine application. The pH of the extracellular recording solution was measured after addition of the different drugs we used, and found to be unchanged at 7.35.

Intrinsic property analysis

The membrane time constant was determined by fitting a single exponential from the start of the current injection to the maximum voltage deflection in a hyperpolarizing

step of -50 pA. The voltage sag was calculated as the percentage difference between the maximum and sustained membrane potential from the first sweep that hyperpolarized the cell to more then -80 mV. Time of voltage sag peak was calculated as the time from the onset of current injection to the maximum voltage deflection. Subsequently the decay time constant of the voltage sag was determined by a single exponential fit from the determined peak to the end of the hyperpolarizing current pulse. A cell was considered to have a voltage sag if the peak exceeded 5% of steady-state voltage. Input resistance was determined by a linear fit through the IV curve of all passive steps. Spike frequency adaptation was calculated from the first sweep where the cell fired >20 Hz on average, by dividing the ninth inter-spike interval (ISI) by the second inter-spike interval. AHP amplitude was determined as the difference between action potential threshold and the minimal potential reached in the repolarizing phase of the action potential (50 ms window). AP threshold was defined as 10 mV/ms in the first derivative of the membrane potential. Action potential height was measured from threshold to the maximal voltage reached. Halfwidth was determined as the full width at half maximal amplitude. Passive and active properties were analyzed using Matlab scripts (Mathworks) and Clampfit (Axon Instruments).

To determine whether the disease history of human patients had an impact on these results, we addressed whether intrinsic properties are affected by the severity of the disease in terms of number of seizures per month, by the time the patients suffered from epilepsy prior to surgery or by disease type (8 patients suffered from mesial temporal sclerosis, 2 from a brain tumor and 1 from cavernoma). With the exception of membrane time constant, we find no such correlations in our data-set, and no significant differences between disease types (**Figure 3D** and **S4**). Moreover, recordings from neurons directly in the epileptic focus, which would be expected to show more severe changes than the neurons in healthy neocortex recorded here,

have suggested no change in action potential threshold (Beck and Yaari, 2008), together indicating that disease history has no major impact on these results.

Unsupervised cluster analysis

To test whether sub-types of L1-INs can be identified, we asked whether electrophysiological parameters can be grouped into distinct clusters. We used Ward's method, because it has no a priori assumption on the number of clusters to be formed. For analysis we used a broad set of electrophysiological properties described in **Figure 3** and **S4**. (Dis)similarity between cells was calculated by determining the Euclidean distance, whereafter cells in close proximity are paired and subsequently grouped into a hierarchical cluster tree. To generate equal weight for the different electrophysiological properties in calculating Euclidean distances, all parameters were first normalized by ranking them between 0 and 1. Cluster analysis was performed in Matlab.

Voltage clamp drug application data analysis

The charge of nicotinic currents was determined by calculating the area under the curve from the start of the current until it decayed back to baseline. Fast and slow nicotinic receptor currents were separated by eye, and post hoc analysis revealed two completely non-overlapping rise slope distributions which differed more than an order of magnitude in size. Together with the results of the pharmacology experiments (Methyllycaconitine citrate, MLA, 10 nM, for antagonizing α7 nAChR and dihydro-β-erythroidine hydrobromide, 1μM, for blocking β2-containing nAChRs), this allowed a reliable classification of fast, slow and biphasic nicotinic receptor compositions. To determine the rise time of the first peak that is mediated by fast α7 receptors, pure α7 and combined biphasic α7/β2 currents were pooled for analysis.

The rise time of β2-mediated currents was quantified on slow monophasic currents, whereas for the decay time pure β2 and α7/β2 currents were combined. For comparability and to avoid influence of the fast component, all β2 decay times were determined starting 400 ms after onset of the current, a time when α7 receptors contribute little to the response (see **Figure S1**). The charge of Htr3 currents was calculated from a fixed 3s interval, to be able to compare it to Htr3 negative cells. Charge and amplitude were calculated using Clampfit (Axon instruments).

In situ hybridization for Htr3a receptors in mouse

Adult mice were anesthetized with 4% isoflurane followed by intraperitoneal administration of ketamine (300 mg/kg) and xylazine (20 mg/kg), and perfused with ice-cold, oxygenated aCSF (in mM): 125 NaCl, 3 KCl, 1.25 NaH2PO4, 3 MgSO4, CaCl2, 26 NaHCO3, and 10 glucose (300 mOsm) for 5 minutes. After removal from the skull, the brain was drop-fixed for 1.5 hours in PLP fixative (4% paraformaldehyde, 5.4% glucose (wt/vol), 0.01 M sodium metaperiodate in lysine-phosphate buffer), washed and stored in RNAse free PBS.

For detection of *Htr3a* mRNA, 30 µm slices were cut from the temporal lobe of the neocortex using a microtome (Leica VT1200 S), and incubated with custom-made hybridization probes (Affymetrix, *Htr3a* receptor, Accession number: NM:001099644; *Htr3a* receptor (negative control), Accession number: NM:013561-N; β-actin, Accession number: NM:007393) followed by amplification steps for detection of labeling. For this we followed the manufacturer's protocol QuantiGene ViewRNA ISH Cell Assay for Fluorescence RNA *in situ* Hybridization (RNA FISH) with a few modifications: Detergent solution was added for 15 min at room temperature and washing steps were increased to 3x10 min.

After probing for mRNA, slices were postfixed (10 min, PLP) and washed three times with 1x PBS. To determine layers and cell depth we stained the slices with mouse anti-NeuN (1:1000, Merck Millipore). Slices were submerged in blocking solution (4% goat serum in 1x PBS), for 1 hour at 21°C, followed by antibody incubation overnight at 4°C. After washing three times with 1x PBS, slices were incubated with secondary antibody (goat anti-mouse Alexa 488, 1:500, Thermo Fisher Scientific), washed again and mounted (Aqua-poly/Mount, Polysciences) on microscope slides.

In situ hybridization for detection of Ndnf in mouse

Adult mice were anesthetized with 4% isoflurane and decapitated. After removal of the skull the brain was placed in a mold, submerged in optimum cutting temperature formulation (Tissue-Tek) and stored at -80 degrees Celsius. Frozen brain sections of 10 µm thickness were made on a cryostat (Leica CM3050 S) and stored at -80 degrees Celsius. In preparation for staining, slices were fixed in PFA (4%), dehydrated, placed in a hydrophobic barrier and pretreated with protease according to the manufacturer's protocol. For detection of *Ndnf* mRNA, slices were incubated with custom-made hybridization probes (Advanced Cell Diagnostics, probe no. 447471-C2, *Ndnf*; 320881, negative control), followed by amplification steps for detection of labeling. For this we followed the manufacturer's protocol RNAscope fluorescent multiplex assay (Advanced Cell Diagnostics). To determine layers and cell depth we stained the slices with DAPI (1:1000, Thermo Fisher) after which they were mounted on microscope slides (EcoMount). We note that while *Ndnf* mRNA was also detected in cells lining blood vessels (c.f. Tasic et al., 2016), our analysis algorithm was designed to exclude these aberrant shapes on the basis of sphericity.

In situ hybridization for NDNF, VIP and HTR3A in human

Due to strong autofluorescence of human brain sections, we performed a chromogenic staining assay on human fresh frozen sections. Upon arrival of the fresh brain samples in the laboratory, they were prepared as described above for mice. In preparation for staining, slices were fixed in PFA (4%), dehydrated, placed in a hydrophobic barrier and pretreated with hydrogen peroxide and protease. For detection of *NDNF*, *VIP* and *HTR3A* mRNA, slices were incubated with custom-made hybridization probes (Advanced Cell Diagnostics, probe no. 495251, *NDNF*; 452751, *VIP*; 310681, *HTR3A*; 310043, negative control) followed by amplification steps for detection of labeling. For this we followed the manufacturer's protocol RNAscope 2.5 HD Detection Reagent - RED (Advanced Cell Diagnostics). To determine layers and cell depth we stained the slices with hematoxylin (50%, Sigma), after which they were mounted on microscope slides (EcoMount).

Imaging and analysis of in situ hybridization

Mouse sections

Imaging was performed using a Zeiss LSM 780/880 confocal laser scanning microscope using a 40x oil objective. Image analysis was done from confocal z-stacks (step size 1 µm). Labeled cells were detected using custom Matlab scripts. Due to the different staining patterns for the different labels (NeuN and *in situ*), two different algorithms were developed: NeuN immunocytochemistry: Due to the high cell density only a subset of the z-stack was used for cell-layer identification from the density of the NeuN staining (mean projection over three consecutive slices). This is the reason why not all *in situ* labeled cells appear in the NeuN-images (**Figure S3**). A band-pass filtered (Gaussian kernel, 1.5 – 10 pixel with 0.4 µm/pixel) version of the image was then thresholded and labeled for object identification. *In situ* hybridization

for *Htr3a* mRNA (see **Figure S3** for an example data set): A maximum projection of the image stack was calculated. A high-pass filter (50 pixels) was applied to compensate for intensity variations across the field of view (e.g. vignetting). In order to distinguish between unspecific background (isolated bright spots) and specific label (local accumulation of spots) and to detect nearby labels as one cell, a number of morphological operations were then applied (image closing (4 pixels), image opening (1 pixel), image closing (10 pixels)). The resulting image was thresholded, the same threshold was applied to samples labeled with anti-sense and sense probes. The resulting binary image was transformed into labeled objects. Object size (minimum number of pixels: 150) and additional object properties (circularity > 0.5, eccentricity < 0.9) were used to further refine the object selection. In order to calculate cell positions relative to the pia, a line was drawn manually along the pia (red line in **Figure S3**). To take the curvature of the pia into account, the depth of each object was calculated as the distance between its center (center of gravity of binary object mask) and the closest point on the “pia-line” (thin white lines in **Figure S3**).

Human sections

The complete mounted slices were scanned on a slide-scanner (PannoramicMIDI, 3DHistech) in transmission mode, and stitched during acquisition using Pannoramic Scan software. Data were exported as RGB tif-files. The locations of pia and of stained cells were marked manually in user-defined subregions. The distance of each cell to the pia was then calculated for each cell (see above, **Figure S3**), cell numbers were binned according to their depth and subsequently converted to cell densities (cells / mm^3) based on the size of the subregion and slice thickness.

Density of Vip *positive interneurons*

Vip-ires-cre mice were crossed with a tdTomato reporter line. From the resulting offspring 3 adult (>8 weeks of age) mice were anesthetized with 4% isoflurane followed by intraperitoneal administration of ketamine (300 mg/kg) and xylazine (20 mg/kg). Mice were perfused with 4% PFA in PBS solution and post-fixed in the same solution overnight at 4°C. Slices of 50 µm were cut on a vibratome, washed 4x in PBS and put in blocking solution (3% BSA, 0.2% Triton in PBS) for two hours. Slices were incubated in blocking solution containing mouse anti-NeuN (1:1000, Merck Millipore) overnight at 4°C. Hereafter, slices were washed 4x with PBS and incubated in blocking solution containing goat-anti-mouse-Alexa488 secondary antibody (Thermo Fisher Scientific) for two hours. After washing 3x in PBS, slices were mounted (HIGHDEF IHC Fluoromount, Enzo Lifesciences) on glass coverslips. For detection of Vip-tdTomato neurons and NeuN stained neurons we used the algorithm described in the *in situ* hybridization section.

Quantification and statistical analysis

Data-sets were first tested for the null hypothesis of normal distribution using the Kolmogorov-Smirnov test. Normally and non-normally distributed data were tested with parametric and non-parametric tests, respectively. Unpaired data sets were tested for significance using a two-sided Kruskal-Wallis test or a two-sided Student's t-test. Paired data-sets were assessed with a one-sided Wilcoxon signed-rank test. Differences in proportions were tested with the Fisher's exact test and the extended Fisher-Freeman-Halton test when evaluating proportions of the three types of nicotinic currents in **Figure 1**. A result was considered significant when the p-value was lower than 0.05. Since effect size was unknown, sample size could not be pre-specified. No randomization procedure or blinding of experimenter was used in the experimental design.

RESOURCE TABLE

REAGENT or RESOURCE	SOURCE	IDENTIFIER
Antibodies		
mouse anti-NeuN	Merck Millipore	MAB377
goat anti-mouse Alexa 488	Thermo Fisher Scientific	A-11001
Chemicals, Peptides, and Recombinant Proteins		
Antisense *Htr3a*	Affymetrix	NM:001099644
Sense *Htr3a*	Affymetrix	NM:013561-N
Antisense B-actin	Affymetrix	NM:007393
Antisense human *NDNF*	Advanced Cell Diagnostics	495251
Antisense human *VIP*	Advanced Cell Diagnostics	452751
Antisense human *HTR3A*	Advanced Cell Diagnostics	310681
Human negative control probe	Advanced Cell Diagnostics	310043
Antisense mouse *Ndnf*	Advanced Cell Diagnostics	447471-C2
Mouse negative control probe	Advanced Cell Diagnostics	320881
Experimental Models: Organisms/Strains		
C57Bl6/J	In house breeding	
Vip-ires-cre	In house breeding	IMSR_JAX:010908
Conditional tdTomato	In house breeding	IMSR_JAX:007909
NDNF-eGFP	In house breeding	MMRRC:030028-UCD
Software and Algorithms		
Matlab	Mathworks	www.mathworks.com
Other		

Supplemental References

Beck, H., Yaari, Y. (2008). Plasticity of intrinsic neuronal properties in CNS disorders. Nat. Rev. Neurosci. *9*, 357-69.

Bennett, C., Arroyo, S., Berns, D., Hestrin, S. (2012). Mechanisms generating dual-component nicotinic EPSCs in cortical interneurons. J. Neurosci. *32*, 17287-96.

Chu, Z., Galarreta, M., Hestrin, S. (2003). Synaptic interactions of late-spiking neocortical neurons in layer 1. J. Neurosci. *23*, 96-102.

Gong, S., Zheng, C., Doughty, M. L., Losos, K., Didkovsky, N., Schambra, U. B., Nowak, N. J., Joyner, A., Leblanc, G., Hatten, M. E., Heintz, N. (2003). A gene expression atlas of the central nervous system based on bacterial artificial chromosomes. Nature *425*, 917-25.

Khawaled, R., Bruening-Wright, A., Adelman, J. P., Maylie, J. (1999). Bicuculline block of small-conductance calcium-activated potassium channels. Pflugers Arch. *438*, 314-21.

Madisen, L., Zwingman, T. A., Sunkin, S. M., Oh, S. W., Zariwala, H. A., Gu, H., Ng, L. L., Palmiter, R. D., Hawrylycz, M. J., Jones, A. R., Lein, E. S., Zeng, H. (2010). A robust and high-throughput Cre reporting and characterization system for the whole mouse brain. Nat. Neurosci. *13*, 133-40.

Squire, L. R., Stark, C. E., Clark, R. E. (2004). The medial temporal lobe. Annu. Rev. Neurosci. *27*, 279-306.

Taniguchi, H., He, M., Wu, P., Kim, S., Paik, R., Sugino, K., Kvitsiani, D., Fu, Y., Lu, J., Lin, Y., Miyoshi, G., Shima, Y., Fishell, G., Nelson, S. B., Huang, Z. J. (2011). A resource of Cre driver lines for genetic targeting of GABAergic neurons in cerebral cortex. Neuron *71*, 995-1013.

Tasic, B., Menon, V., Nguyen, T. N., Kim, T. K., Jarsky, T., Yao, Z., Levi, B., Gray, L. T., Sorensen, S. A., Dolbeare, T., Bertagnolli, D., Goldy, J., Shapovalova, N., Parry, S., Lee, C., Smith, K., Bernard, A., Madisen, L., Sunkin, S. M., Hawrylycz, M., Koch, C., Zeng, H. (2016). Adult mouse cortical cell taxonomy revealed by single cell transcriptomics. Nat. Neurosci. *19*, 335-46.

Testa-Silva, G., Verhoog, M. B., Linaro, D., De Kock, C. P., Baayen, J. C., Meredith, R. M., De Zeeuw, C. I., Giugliano, M., Mansvelder, H. D. (2014). High bandwidth synaptic communication and frequency tracking in human neocortex. PLoS Biol. *12*, e1002007.

Verhoog, M. B., Goriounova, N. A., Obermayer, J., Stroeder, J., Hjorth, J. J., Testa-Silva, G., Baayen, J. C., De Kock, C. P., Meredith, R. M., Mansvelder, H. D. (2013). Mechanisms underlying the rules for associative plasticity at adult human neocortical synapses. J. Neurosci. *33*, 17197-208.